Submarine Platform Development by Erosion of a Surtseyan Cone at Capelinhos, Faial Island, Azores

Zhongwei Zhao[1*], Neil C. Mitchell[1], Rui Quartau[2, 3], Fernando Tempera[4, 5], and Lucy Bricheno[6]

[1]Department of Earth and Environmental Sciences, University of Manchester, Williamson Building, Oxford Road, Manchester M13 9PL, UK.

[2]Instituto Hidrográfico, Divisão de Geologia Marinha, Lisboa, Portugal.

[3]Instituto Dom Luiz, Faculdade de Ciências da Universidade de Lisboa, Lisboa, Portugal.

[4]Centro do IMAR da Universidade dos Açores, MARE – Marine and Environmental Sciences Centre, Rua Prof. Dr. Frederico Machado, 4, 9901-862 Horta, Açores, Portugal.

[5]IFREMER, Centre de Bretagne, DYNECO-LEBCO, CS 10070, 29280 Plouzané, France.

[6]National Oceanography Centre, Joseph Proudman Building, 6 Brownlow Street, Liverpool L3 5DA, UK

*zhongwei.zhao@manchester.ac.uk; zzw920219@gmail.com

Key words: submarine platform, coastal erosion, Surtseyan eruption, wave attenuation, Azores

Abstract

Erosion of volcanic islands ultimately creates shallow banks and guyots, but the ways erosion proceeds to create them over time and how coastline retreat rate relates to wave conditions, rock mass strength and other factors are unclear. The Capelinhos volcano was formed in 1957/58 during a Surtseyan and partly effusive eruption that added a ~2.5 km^2 tephra and lava promontory to the western end of Faial Island (Azores, central North Atlantic). Subsequent coastal and submarine erosion has reduced the subaerial area of the promontory and created a submarine platform. This study uses historical information, photos and marine geophysical data collected around the promontory to characterize how the submarine platform developed following the eruption. Historical coastline positions are supplemented with coastlines interpreted from 2004 and 2014 Google Earth images in order to work out the progression of coastline retreat rate and retreat distance for lava- and tephra-dominated cliffs. Data from swath mapping sonars are used to characterise the submarine geometry of the resulting platform (position of the platform edge, gradient and morphology of the platform surface). Photographs collected during SCUBA and ROV dives on the submarine platform reveal a rugged surface now covered with boulders. The results show that coastal retreat rates decreased rapidly with time after the eruption and approximately follow an inverse power law relationship with coastal retreat distance. We develop a finite-difference model for wave attenuation over dipping surfaces to predict how increasing wave attenuation contributed to this trend. The model is verified by reproducing the wave height variation over dipping rock platforms in the UK (platform gradient 1.2° to 1.8°) and

Ireland (1.8°). Applying the model to the dipping platform around Capelinhos, using a diversity of cliffs resistance predicted from known lithologies, we are able to predict erosion rate trends for some sectors of the edifice. We also explore wider implications of these results, such as how erosion creates shallow banks and guyots in reef-less mid-oceanic archipelagos like the Azores.

1. Introduction

Submerged banks are common in volcanic archipelagos like the Azores. During periods of their evolution when they were islands or shallow banks they affected wave propagation (Arthur, 1951; Ponce de León and Guedes Soares, 2005), and were therefore important for inferring how wave conditions varied amongst the islands. At human time scales, quantifying such coastal erosion is necessary for planning purposes as waterfront properties and other infrastructures are commonly valuable assets of steep volcanic islands. Finally, from a biological perspective, understanding how long isolated islands survived before becoming submarine banks is also important, as coasts and shallow bottoms constitute critical stepping stones permitting long-distance species colonisation to occur by shorter stages (Whittaker, 1998).

Extensive field experiments and numerical modelling have explored and advanced our knowledge on how width, gradient and roughness of near-shore rock platforms affect wave dissipation and transformation (Trenhaile, 2000; Madin et al., 2006; Farrell et al., 2009; Sunamura et al., 2014; Poate et al., 2016; McCall et al., 2017; Poate et al., 2017). Although the factors affecting erosion are weakly constrained, modelling efforts have successfully reproduced the geometries of resulting rock platforms (e.g., Trenhaile, 2000). However, observations of coastal

retreat history in areas with varied lithology and wave conditions are rare, but are needed in order to refine coastline change models. Improving our understanding of the roles of wave exposure, resistance to erosion, seaward transport of eroded material and other factors could help us to improve predictions of retreat rates of rocky coasts more widely.

Coasts formed by historical volcanic activity provide an opportunity to observe the geomorphological effects of erosion at timescales ranging from the months following the end of eruption to periods reaching several decades. Surtseyan cones in exposed oceanic settings constitute exceptional fast-evolving case studies of coastal development (Quartau, 2010; Ramalho et al., 2013; Quartau et al., 2014; Romagnoli and Jakobsson, 2015).

In Surtseyan eruptions, explosive interactions of lava with water create friable volcanoclastic material (Moore, 1985; Kokelaar, 1983). In the case of Surtsey Island, the eruption produced a subaerial cone of such material that eventually isolated the vent from seawater, allowing lava to start extruding non-explosively (Thorarinsson, 1967; Thorarinsson, 1968). In Surtsey and other similar cones, the earlier friable material was easily eroded by surf, whereas later erupted lavas and palagonitized tephra were more resistant to erosion (Kokelaar and Durant, 1983; White, 1996; Cole et al., 2001; Murtagh and White, 2013; Romagnoli and Jakobsson, 2015; Ma et al., 2018). The poorly-consolidated materials making up Surtseyan cones can be efficiently mobilised by wave erosion and give rise to shallow marine platforms on timescales that are rapid compared with other environments (Romagnoli and Jakobsson, 2015), hence making studies possible, as here, using historical data.

The Capelinhos cone was emplaced as a typical Surtseyan cone (Cole et al., 1996; Cole et al., 2001) on the western-most end of Faial Island (Figure 1a) by an

eruption extending over 13 months (September 1957 - November 1958) (Machado et al., 1962; Cole et al., 1996; Cole et al., 2001). Borges (2004) quantified the Capelinhos rate of shoreline retreat until the year 1981 by assessing post-eruptive coastal development (Machado and Freire, 1985). His rates were averaged over the whole promontory, whereas in practice the lithology of Capelinhos coast varies along the coast. Although he provided no detailed explanation, he highlighted how the high retreat rates that immediately followed the eruption subsequently declined.

In this study, we have quantified coastal retreat rates for the Capelinhos promontory (from August 1958 to November 2014) based on historic coastline positions extracted from topographic maps and aerial images. The rates were quantified in a series of sectors with different lithology and orientation (hence wave exposure). Submarine geophysical data including multibeam and other sonar bathymetry and Chirp shallow seismic profiles provide information on the morphology and nature of the submarine feature carved by erosion. We describe the resulting submarine feature as a “platform” - a term, more typically used to describe the result of coastal erosion of more rigid rocky material over longer periods. We further compared the coastline retreat rates with the history of wave conditions. We have developed a finite difference model to predict how wave erosive force in front of the cliff varies with platform width, platform gradient, cliff resisting force and deep-water wave heights using wave attenuation models and have verified it using wave data. The combined approach has allowed us to investigate how and why the shoreline retreat rate changed with time after the eruption and how it affected the subaerial and submarine morphology of the promontory. We further discuss implications of the results to how some shallow banks are created by coastal erosion.

2. Regional Setting

2.1 Geological setting

The Azores archipelago comprises nine volcanic islands generally lying along a WNW-ESE trend in the centre of the North Atlantic Ocean. Faial Island lies in the central group of the islands, 130 km to the east of the Mid Atlantic Ridge (Figure 1b). It is 21 km long (WNW-ESE) and 14 km wide. Its highest peak reaches 1043 m above sea level (Madeira et al., 2015).

The Capelinhos volcano, in the western-most promontory of Faial, was formed within the Capelo rift zone that prolongs Faial to the WNW (Romer et al., 2018). According to the seabed contour map of Machado et al. (1959), which is based on a British Admiralty sounding chart, there was a submarine platform at Capelinhos before the eruption. That platform likely resulted from erosion of the earlier Costado da Nau cone, whose remnants are still visible in cliffs east of Capelinhos. Two small islets also existed prior to the Capelinhos eruption and were buried by it (these are presently being unearthed again by erosion). The depth and extent of this earlier platform unfortunately cannot be reliably reconstructed.

The eruption started underwater on 27th September 1957 and comprised three major phases of Surtseyan activity (Cole et al., 1996, 2001). Phase I lasted one month (September to October of 1957) and comprised hydromagmatic activity (Figure 2.a-b). Phase II, extending two months from November to December of 1957, included hydromagmatic activity and two days of discharge of lava flows (Figure 2.c-d). Phase III started in January 1958 with hydromagmatic activity and lasted four months (Figure 2.e-h). These phases were followed by additional lava discharges from late April 1958 until the end of the eruption in November 1958 (Figure 2.i-l), with flows covering some sectors of the tephra deposited by earlier

phases (Machado et al., 1962; Waters and Fisher, 1971; Cole et al., 1996; Cole et al., 2001). The physiographic and lithological evolution of Capelinhos during the eruption was well characterised by Machado et al. (1959) (Figure 2). They described how the eruption started underwater (Figure 3a) and was followed by an early phase of violent submarine explosions of gas, steam and black tephra ash (Figure 3b) that eventually gave rise to an emerged cinder ring (Figure 3c). The activity subsequently transitioned from Surtseyan to Strombolian as the cinder ring worked as a barrier isolating the vent from seawater (Figure 3d). The final shape of the Surtseyan cone was settled at the end of the eruption (Figure 3e) and has since been modified by wave erosion (Figure 3f, Machado et al., 1962; Cole et al., 1996; Cole et al., 2001).

The first (westernmost) tephra cone was dismantled by seaward collapses over 8 days in late October 1957. Frequent landslides and a partial collapse destroyed the remaining tephra cones (Cole et al., 1996; Cole et al., 2001) until lava flows emplaced in 1958 on the eastern side of Capelinhos fortified the third and last spatter cone.

By the end of the eruption, a total ~2.5 km^2 land area had been produced and the edifice reached ~160 m above sea level (Machado et al., 1962). Based on topographic maps, Machado et al. (1959) estimated the volume of erupted tephra and lava reached ~0.15 km^3, of which 56% was lava and 44% tephra. The tephra was mainly deposited from ash fallout and pyroclastic surges produced by subaerial and submarine explosions (Cole et al., 2001). Waters and Fisher (1971) characterised the continuously-bedded tephra layers, which vary significantly in clast size from finely-sorted and densely-graded impalpable dust to poorly-sorted, unconsolidated and coarse layers containing fragments exceeding ~50 cm in size. Abundant lava chips and blocks also occur. Olivine basalt lavas with varied viscosity

flowed over the west and north flanks of the cone, with a larger volume to the northwest. A broad subaerial platform was then built along the seaward rim of the Capelinhos volcano, with most lava flows penetrating the sea (Machado et al., 1962). However, a lava flow emplaced on 23rd August 1958 fed by a feeder dyke immediately below the Capelinhos lighthouse (Figure 2k) failed to enter the sea (Cole et al., 2001).

From the coastline evolution of Machado et al. (1959), significant erosion of the seaward lava platform occurred and new beaches of volcanic ashes formed in June 1959 in the northeast and south. During the visits of Cole et al. (1996) in 1994 and 1995, the lava flow emplaced below the lighthouse (Figures 2k-2l) had become exposed to sea erosion. Large angular lava boulders resulting from the dismantling of the lava flow were found on the underlying southern beach. By 2007, the area of Capelinhos had been reduced to ~0.565 km^2 as a consequence of wave erosion, landslides, wind, precipitation and actions of visitors to the site (Forjaz, 2007; Forjaz et al., 2010).

2.2 Oceanographic setting

Faial Island is exposed to high-energy swells generated by distant storms in the Atlantic and to waves created by local winds. Their propagation through the islands has been modelled by Rusu and Soares (2012). The nearest windward lands to Faial are Flores and Corvo (Figure 1b) which lie ~234 km to the WNW and represent only a minor interference to the prevailing swells hitting Faial from the west or northwest. The deep water surrounding the Azores islands and their narrow shelves imply that waves experience little attenuation before reaching the coasts when compared with continental shelf environments (Rusu and Soares, 2012).

Wave hindcast data presented in Carvalho (2003) for the period 1989-2002 suggest that the prevailing swells impinge Faial from the northwest (29%) and west (24%), with monthly-averaged offshore wave heights ranging between 1 and 4 m (with stronger wave conditions in winter than in summer). Violent storms associated with extratropical storms or hurricanes affect the Azores every 7 years on average (Andrade et al., 2008), a frequency mainly dominated by the North Atlantic Oscillation and partially affected by Eastern Atlantic atmospheric circulation. They bring extreme waves to Faial with heights exceeding 16 m and peak periods exceeding 18s (Quartau, 2007). “Christina” (also called storm “Hercules”) was the latest extreme cyclone to approach the Azores archipelago (5-7 January, 2014). The waves generated reached 9-11 m (Melo et al., 2018) and significantly damaged coastal structures (Santos et al., 2014). Faial’s mean annual tidal range is only ~0.9 m (Quartau et al., 2012), which corresponds to a microtidal regime (Short, 1996).

3. Materials and methods

3.1 Coastal change

We digitised the shoreline positions of November 1958, May 1959, July 1964, September 1975 and March 1981 from the maps of Machado and Freire (1985). The coastlines of November 2004 and October 2014 were interpreted and digitised from Google Earth images (google.com/earth). The coastlines are shown in Figures 4 and 5 georeferenced using a Universal Transverse Mercator projection (UTM, zone 26N). The Root Mean Square Errors (RMSEs) of georeferencing and digitizing were estimated using the georeferencing tool in ArcGIS to be 11–41 m (Table A1). In the following, we refer to elapsed time from the first map of the sequence following the eruption (November 1958).

Machado et al. (1959) classified the coasts as lava- and tephra-dominated. We have slightly extended their classification, using lava, tephra and mixed lava and tephra ("lava+tephra") classes. They were further divided them by location (north or south) resulting in a total of six sectors (Figure 5).

Areal changes were derived from the plan-view polygons lying between historical coastline positions, and laterally delimited by the sector boundaries (key in Figure 5). In each polygon, the lengths of coastline at dates T_a and T_b were measured as L_a and L_b (Table A2). The average coastline length L' for this time interval ($\Delta T=T_b-T_a$) was then derived from $L'= 0.5*(L_a+L_b)$. The areal change produced by erosion ΔA in time interval ΔT was measured using ArcGIS. From these values, the average incremental costal retreat rate of each sector $\Delta D=\Delta A/L'$ and its average retreat rate $R_r= \Delta D/\Delta T$ were determined. The total coastal retreat distance $D=\sum\Delta D$ was also determined. The above calculations were conducted separately in the different sectors (Table 1). By repeating the measurements and calculations, the following uncertainties were estimated: L, ~5%; ΔA, ~3%; ΔD, ~8% and R_r, ~10% (including date uncertainty).

As the early coastline evolution was poorly characterised in both Capelinhos and Surtsey, we have studied this stage by resorting to a series of remote-sensing images (Appendix 4) of the Sholan Island (Red Sea), which erupted from 18 December 2011 (Xu et al., 2015). Although wave conditions are different in the Red Sea, and therefore rates will be different, those data suggest a different form of early coastal retreat distance with time and R_r with D.

3.2 Submarine geomorphology

Data from two bathymetric surveys were used to characterise the submarine

245 platform created by wave erosion. Deeper sections (depths 19 m to 216 m) were
246 surveyed in 2003 (Mitchell et al., 2008) using a Reson 8160 multi-beam sonar. The
247 near-shore area (depths 2 m to 77 m) was mapped with a Submetrix interferometric
248 swath sonar in 2004 (Tempera, 2008) (Figures 1a and 6a). Both datasets were
249 processed with tidal and attitude corrections and combined into a 5 m resolution grid
250 (Tempera, 2008) in UTM coordinates (zone 26N). Six bathymetric cross-sections
251 were selected to characterise the morphology of the submarine platform as shown in
252 Figure 6b. Some geometrical characteristics of these profiles are summarized in
253 Table 2. From these profiles, the positions of the platform edge were interpreted from
254 where seabed gradient changed prominently. They are marked by the orange circles
255 on the bathymetric profiles and vertical dashed orange lines in Figure 6b. Platform
256 width *W* was measured as the horizontal distance between the platform edge and
257 the present coastline. As the repose angle of loose volcanic talus is ~30° (Mitchell et
258 al., 2000; Mitchell et al., 2012a), a possible geometry of the initial shallow submarine
259 slope can be represented by a surface running from the earliest post-eruption
260 coastline position at a 30˚ dip, as shown by the dipping dashed lines in Figure 6b.
261 Uncertainty in this early slope surface arises because the coastline position
262 immediately at the end of the eruption may not have been recorded exactly by the
263 maps of Machado and Freire (1985) and wave agitation may have caused the
264 volcanic material to deposit at a gradient smaller than the angle of repose.
265 Nevertheless, comparing this surface with the platform edge in the geophysical data
266 give us a possible measure of how much the platform edge has prograded by
267 material re-deposition. For comparison with the subaerial eroded volume, the
268 approximate volume of sediment deposited at and below the platform edge was
269 estimated by measuring and averaging the area of sediment deposition in each

sector and then multiplying by the November 1958 coastline length.

The three high-resolution seismic profiles shown in Figure 6c were collected in 2001 with a 1.5–10 kHz Chirp source across the submarine platform (Quartau, 2007) and illustrate its surficial morphology. Interpretation of the data followed the method of Quartau (2007) but was simplified to separate the rugged and smooth morphologies.

The seabed images shown in Figure 7 were acquired in 2004/2005 using Remotely Operated Vehicle (ROV) and SCUBA divers at locations S1 and S2 marked in Figure 6a. As no underwater acoustic positioning system was available, the photographs were located using GPS recordings of the research vessel position (Tempera, 2008). Photograph depths were not recorded, but were estimated from the bathymetric map to be ~38 m (ROV) and ~10 m (SCUBA dives).

3.3 Wave conditions

Using the hindcast data of Carvalho (2003), a rose diagram for offshore wave heights and their associated percentages and originating directions was produced (Figure 8a). We further characterised the wave properties during times when significant wave heights exceeded 5 m (Figure 8b), as 5 m is the minimum wave height for broken wave to exceed the threshold of erosion of less resistant cliff material (tephra) to initiate coastal erosion (Sunamura, 1992). (This 5 m value is further justified in Appendix 6.)

The European Centre for Medium range Weather Forecasts (ECMWF) 40-yr Re-Analysis (ERA-40) (Uppala et al., 2005) and ECMWF interim Re-Analysis (ERA-Interim) (Dee et al., 2011) are reconstructions of sea surface and meteorological conditions from a numerical model using meteorological observations as inputs.

These ERA model outputs have been shown to be reliable when compared against local wave buoy data collected in deep-water and for some coastal settings where waves are not shadowed by adjacent coasts (Caires and Sterl, 2003; Sterl and Caires, 2005; Mitchell et al., 2012b) as is the case of the fully-exposed shore of Capelinhos for waves not propagating from the east. ERA outputs of wave properties were extracted for a sea position adjacent to Capelinhos (38.625°N, 28.875°W) for the period 1957 to 2016 (60 years). In order to represent the properties of the most extreme waves, wave heights observed during each year were sorted and only the upper 5 percentile was retained. The mean and range of those heights are shown in Figure 9, and compared with historical coastal retreat rates. Appendix 7 shows the corresponding periods of these waves along with an analysis of extreme waves based on extreme value theory.

3.4 Coastal lithological observation

Capelinhos was visited on 5th and 6th July 2017 to make detailed observations from shore (Figures 10a, 10b, 10d and 10f), and combined with earlier observations by author F.T. in January 2011 from offshore (Figure 10c) and on land (Figure 10e). The rock mass strength of lava boulders protecting coastal cliffs in the south was assessed during the 2017 visit using a HT-225B concrete rebound test Schmidt hammer. The equipment was tested prior to fieldwork on a large steel object, returning a rebound value of 78, which is within the range of values (80 ± 2) that the manufacturer suggests should be obtained on steel anvils. In total, 30 measurements were taken using the Schmidt hammer along the south Capelinhos lava cliffs (located in Figures 10b and 10g). A further test after the fieldwork on the same large steel object produced again a value of 78. Schmidt hammer rebound

values (R) were converted to rock comprehensive strengths (S_c) using the equation of Kahraman (2001) as suggested in Sunamura et al. (2014):

$$S_c = 6.97e^{0.014\rho R} \quad (1)$$

where ρ is the rock density of cliff material in g/cm^3.

Machado et al. (1962) estimated the density of lava and tephra from Capelinhos eruption as 2.6 g/cm^3 and 1.1 g/cm^3 respectfully. We then averaged these rock densities to derive a density for lava+tephra sector cliffs (1.85 g/cm^3). No Schmidt hammer tests were possible on the tephra coast, so the average Schmidt hammer rebound value of 35 for tephra from Kahraman (2001) was used. The value of 45 for lava+tephra sectors was then derived from the average of the above values for lava and tephra materials. The calculated compressive strength S_c of lava, tephra and lava+tephra (appendix 6) was then used in the following numerical modelling section.

3.5 Wave height attenuation

A finite difference model was developed to predict how wave height is reduced by attenuation when crossing the dipping platforms. Within the model, we idealise a dipping platform with a series of very small horizontal steps (Figure 11) and apply attenuation rates from equations of Sunamura et al. (2014) to work out the small reduction in wave height across each step. Integrating the effect of those rates with varying water depth yields wave height at the coastline. This is a simpler approach than that used by McCall et al. (2017), which considered effects of finer-

345 scale bed topography, as our data are insufficient to constrain roughness in earlier
346 stages of the platform development. Although the equations of Sunamura et al.
347 (2014) were derived from wave attenuation measurements across nearly flat
348 platforms, we assume here that they will faithfully represent the attenuation in small
349 steps where the variation in depth is very small across each step. The tests of the
350 model employ the wave data of McCall et al. (2017), which apply only to shallow
351 dipping platforms (1.2˚ to 1.8˚), so the model has not yet been tested with wave data
352 on more steeply dipping platforms. Nevertheless, wave attenuation will be much
353 smaller over the more steeply dipping platforms (e.g., 30˚) where the water depth is
354 larger, so we suggest the model should still capture the contrasting effects of steep
355 and shallow platforms.

356 Using field measurements of wave height across a horizontal reef surface
357 (Madin et al., 2006), Sunamura et al. (2014) proposed the following equations to
358 represent wave attenuation over a horizontal platform:

359 $$\frac{H}{H_e} = \alpha\left(e^{-\beta X} - 1\right) + 1, \quad (2)$$

360 $$\alpha = exp\left[-0.016\left(\frac{h}{H_e}\right)^4\right], \quad (3)$$

361 $$\beta = 0.030\ exp\left[-0.70\left(\frac{h}{H_e}\right)\right], \quad (4)$$

362 where H is the attenuated wave height at a distance X from the platform edge, H_e is
363 the wave height at the platform edge, α is a dimensionless coefficient and β is a
364 decay coefficient (Sunamura et al., 2014). Values for α and β were determined from
365 data of Ogawa et al. (2012).

366 These Sunamura et al. (2014) equations were derived from wave data on
367 sub-horizontal shore platforms (gradient <1˚). Each cell has width d in X and the
368 number of cells n is related to the platform width W, $n = \frac{w}{d}$. The attenuated wave

height at the landward end of each cell (e.g. H_j in Figure 11) was used as the input value for the seaward end of the next cell (e.g. H_{i+1} in Figure 11). The calculation was repeated for each model cell until reaching the coast.

In one form of the model, we varied the gradient of platform from θ_a to θ_b while varying the platform width from w_a to w_b. The platform width at intermediate stages w_k ($w_a \leq w_k \leq w_b$) is then linearly related to the gradient of platform: $\theta_k = \theta_a - \left(\frac{w_k - w_a}{w_b - w_a}\right)(\theta_a - \theta_b)$.

The equations of Sunamura et al. (2014) were adapted as follows for cell i ($0 \leq i \leq n-1$), which has its seaward edge at X_i m from the dipping platform edge:

$$\frac{H_j}{H_i} = \alpha_i\left(e^{-\beta_i d} - 1\right) + 1, \tag{5}$$

when $\frac{h_i}{H_i} < 1$:

$$\alpha_i = 1, \tag{6}$$

when $\frac{h_i}{H_i} \geq 1$:

$$\alpha_i = exp\left[-0.016\left(\frac{h_i}{H_i}\right)^4\right], \tag{7}$$

$$\beta_i = 0.030\ exp\left[-0.70\left(\frac{h_i}{H_i}\right)\right], \tag{8}$$

$$h_i = (w_k - X_i)\ tan\,\theta_k, \tag{9}$$

$$X_i = (i-1)d. \tag{10}$$

where α_i is a dimensionless coefficient and β_i is a decay coefficient, H_j is the attenuated wave height at the landward edge of cell i, H_i is the wave height at the seaward edge of cell i. When i =0, H_i=H_e which is the initial wave height at the dipping platform edge. H_j equals to the attenuated wave height at the coastline when i=n-1(H_j =H_n). h_i is the water depth of the seaward edge of the cell and, as the cell is horizontal, it is also the depth for the cell.

For verification purposes, the model was run using the platform seaward edge wave heights and platform dips derived from the data of Poate et al. (2017) and McCall et al. (2017) for some topographically rough dipping platforms in shallower water. Running the model with the wave heights shown along the left of each panel in Figure 12, using the platform dips shown, resulted in the model outputs (cell size: 0.5 m). The model fits the training observations with average RMS misfits (wave height minus model predicted height) of only 6 cm. Note that there were no free parameters set during this procedure.

The geometrical conditions more appropriate for Capelinhos were chosen based on the platform geometry in Figures 6b and 6c (600 m width, 3° dip for fixed gradient platform and 30° varied to 3° dip for varied gradient platform). Extreme wave heights of 8 m were used as explained in section 3.3 (other wave heights of 6, 10 and 12 m were also used to simulate attenuated wave heights across a dipping platform with the varied wave heights at the platform edge in Figure 13c). Attenuated wave height at different distances from the coast was simulated for uniformly dipping platforms with different total width, dip and initial wave height, producing the results shown in Figure 13.

Sunamura (1977) suggested that the cliff erosion rate *dD/dt* should be proportional to the wave erosive force *F*:

$$\frac{dD}{dt} = CF \tag{11}$$

where *D* is the eroded distance, *t* is the elapsed time of erosion and *C* is the constant of proportionality. Dimensionless parameter *F* (unit less) was defined by Sunamura et al. (2014) as:

$$F = \frac{F_W}{F_R} - 1 \qquad \text{for } F_W > F_R \tag{12}$$

$$F = 0 \qquad \text{for } F_W \leq F_R \tag{13}$$

where F_W is the wave assailing force (N/m^2 or Pa) and F_R is the cliff resisting force given by:

$$F_W = A\rho g H_f \tag{14}$$

$$F_R = BS_c \tag{15}$$

H_f (m) is the wave height in front of the cliff, S_c is the compressive strength of the cliff materials (MPa), ρ is the density of sea water (1025 kg/m^3), g is the gravitational acceleration (9.8 m/s^2), and A and B are dimensionless coefficients that are related:

$$k = \frac{A}{B} \tag{16}$$

where k is a coefficient equal to 667 for breaking waves and 250 for broken waves. Sunamura et al. (2014) combined equations (12) to (16) to produce:

$$F = k\left(\frac{\rho g H_f}{S_c}\right) - 1 \qquad \text{for } F_W > F_R \tag{17}$$

Both breaking and broken waves can attack the shore and determining which are the more important is difficult. We therefore used both equations (13) and (17) to calculate the erosive force for both breaking and broken waves (using different k values in equation (16)) in Figures 13e and 13h from the attenuated wave heights in front of the cliff shown (at 0 m distance) in Figures 13d and 13g. The results are shown in Figures 13f and 13i with logarithmic axes to expose whether they suggest power-law trends comparable with the coastline retreat rates described later. Wave height (Appendix 8) and erosive force (Appendix 8 and Figure 14) for six different coastal sectors were also simulated using similar method as for Figure 13.

438 ## 4. Results

439 ### 4.1 Field observations of the modern coastlines

440 Owing to the rapid on-going wave erosion, the lithology of exposed cliffs, their
441 joint intensity and consequently their rock strength (i.e., cliff resisting force F_R) have
442 changed both spatially and temporally (Cole et al., 2001).

443 In the tephra south sector, the presently exposed southwest cliff comprised
444 bedded submarine pyroclasts (ashes) (Figure 10a) at the time of our visit with a
445 narrow and low gradient sandy beach in front of the cliff base. These submarine
446 pyroclasts were friable and too weak to conduct Schmidt hammer measurements.
447 The pre-eruption lava sea stacks presently exposed in the southwest edge of
448 Capelinhos are marked in Figure 10a. Their base contains submarine pyroclasts
449 according to Forjaz (2007). During our visit, they appeared to contain few fractures,
450 helping to explain their persistence.

451 The basaltic lava flow emplaced on 23rd August 1958 below the Capelinhos
452 lighthouse is presently exposed in south Capelinhos and possibly originally fed by
453 the dyke marked in Figure 10b. Large lava boulders (mean diameter >1.5 m) lie at
454 the cliff base and appear to temporarily armour it in a way similar to rock armour in
455 coastal engineering. These were likely formed by undermining of the lava flow by
456 wave erosion and collapses of the overlying material. The Schmidt hammer
457 measurements conducted on these basalt blocks produced a mean rebound value of
458 55. Using equation (1), their comprehensive strength is 51.6 MPa.

459 The presently exposed cliff of lava south and lava+tephra south sectors were
460 observed from land and offshore (Figures 10c and 10d). They comprise basaltic lava
461 flows that have low joint density in their lower section, while their top section
462 comprises reddish (iron rich) subaerial pyroclasts (scorias and ashes). A narrow

463 beach (Figure 10d) was found in the lava+tephra coast with pebble-sized clasts of
464 the cliff materials. Unfortunately, the presently exposed lava and lava+tephra north
465 cliffs are inaccessible from land and we have very limited offshore observations of
466 them (Figures 10e and 10f).

467 The presently exposed cliff of the tephra north sector (Figures 10e and 10f) is
468 similar to the southwest Capelinhos cliffs and comprises submarine pyroclasts
469 (ashes). A low gradient sandy beach was found in the base of the cliff. Its northwest
470 edge was topped by pyroclasts blocks caused by recent collapse (the scar of the
471 collapse is indicated in Figure 10f). In 2011, these collapsed materials were
472 observed forming a talus deposit at the cliff base (Figure 10e).
473

474 4.2 Historical variation of coastal position

475 Marine erosion has reduced the area of the Capelinhos promontory from ~2.5
476 km^2 in 1958 to ~0.42 km^2 in 2014. As shown in Figure 9, all coastlines retreated
477 rapidly in the first year following the eruption and progressively less rapidly since
478 then, though with notable variations between sectors and lithologies (Table 1), some
479 of which we highlight below. The coastal retreat rates plotted logarithmically against
480 coastal retreat distance in Figure 15b reveal that the data form almost inverse power
481 law relationships. Deviations from those power laws reveal anomalies relative to the
482 overall erosional trends, e.g., intervals of unusually fast erosion. The power law
483 gradients also vary between sectors (Figure 15c), implying varied decelerations of
484 retreat rates.

485 The highest retreat rate ~326 m/yr occurred in the lava+tephra north sector (in
486 Figure 9) 08/1958 to 05/1959 (month/year), when the rates for other sectors were
487 only ~17% (tephra north) to 61% (lava south) of that highest value. In three cases,

short-lived increases of retreat rates were found, violating the general decreasing trends. Two of them occurred in the interval 03/1981-11/2004, which followed the interval 09/1975-03/1981 when no coastal retreat had occurred (lava north and lava south sectors). The third occurred in the tephra north sector during 09/1975-03/1981. Retreat rates for the different sectors all eventually decreased to ~1-3 m/yr by 10/2014, while some of them decreased to and maintained ~2 m/yr (lava+tephra south sector since 1975 and tephra south sector since 1981).

In all sectors, the retreat rates decreased rapidly with time after the eruption, tending towards a more constant and slower rate after a few decades (Figure 9). This is consistent with the suggestion of Trenhaile (2000) that rock platforms formed by wave erosion tend towards a state of equilibrium because of increasing wave attenuation. The retreat rates derived from coastline retreat distances were ~46% faster on the northern coast than on the southern coast between 1958 and 2014.

4.3 Submarine morphology of the platform

The geophysical data reveal the morphology of the gently seaward-dipping submarine platform potentially resulting from wave erosion.

4.3.1 Platform geometry

The profiles selected to represent sectors with different lithologies reveal varied platform geometrical features (Table 2). In Figure 6b, the interpreted platform edge in all profiles lies seaward of the earliest (1958) shoreline position recorded, though by distances varying from 100 to 300 m. The platform is widest in the lava+tephra north sector (profile B3), where it is 832 m wide. In the lava north (profile B2) and tephra north (profile B1) sectors, the platform is narrower, 703 m and 533 m,

512 respectively. In the southerly sectors, the platform is narrower than in the north with
513 same lithologies. The platform in the lava+tephra south sector (profile B5) is the
514 narrowest at 383 m. The platform lava south (profile, B4) and tephra south (profile
515 B6) sectors are intermediate in width, at 541 m and 475 m, respectively.

516 The platform dips are generally 3° (Table 2), though vary from 2° for the
517 lava+tephra north platform to 5° for the lava+tephra south platform. The depth of the
518 platform edge is between 14 and 59 m (Table 2). The average depth (33 m) is
519 comparable with the 45 m depth of Surtla, a cinder edifice also produced by
520 Surtseyan activity and eroded by waves over a period of 18 years (Kokelaar and
521 Durant, 1983).

522

523 4.3.2 Seabed morphology in Chirp data

524 The submarine platform is rugged in the Chirp profiles (“rugged” in Figure 6c),
525 corresponding to a surface of angular boulder to pebble-sized clasts visible in the
526 photos (Figure 7). Metre-sized lava boulders have probably moved off the paleo-
527 coastline by rolling or sliding. Below the platform edge, the seabed is smoother,
528 which we interpret as caused by finer sediment deposits (“smooth” in Figure 6c). The
529 surface rugosity (Figures 1 and 6a) is different between the northern part of the
530 platform adjacent to the tephra and the southern part adjacent to the tephra (it is
531 smoother in the north than in the south).

532 A ridge marked in Figure 1a crossing the platform WNW to ESE is interpreted
533 as a volcanic dyke remnant (ridge left after erosion). It is aligned with the
534 Capelinhos vents and most of the scoria cones of west Faial Island, which also lie
535 WNW-ESE (Cole et al., 2001). A low relief escarpment, ~300 m from the southwest

536 coast in Figure 1a, runs NW-SE and very close to the 1958 coastline of Figure 4.
537 We suggest the top of this escarpment is the platform edge corresponding to the
538 1958 eruption, while the platform seaward of it is a pre-existing platform as marked
539 in Figure 1a.
540

541 ## 4.4 Interpretation

542 ### 4.4.1 Subaerial

543 From the observations of Machado et al. (1959), the lava sectors were initially
544 developed by lava emplaced over the tephra, so their bases are likely tephra-
545 dominated. Undermining by removing their tephra bases explains their rapid cliff
546 retreat. However, large angular lava boulders deposited at the base of the cliffs by
547 collapse of the overlying lava (Cole et al., 1996; Figure 10b) temporarily armoured
548 and likely slowed wave erosion of the cliffs. This armouring might also explain the
549 lack of retreat in the lava coastal sectors from 09/1975 to 03/1981 (Figure 9).

550 The lava+tephra north-western sector of the headland is fully exposed to
551 prevailing swells (Figure 8). These areas also sheltered the southern and eastern
552 sectors from the westerly and north-westerly swells. The greater exposure of
553 northern and western coasts resulted in their larger coastal retreat distances (Figure
554 9).

555 Slow retreat of the tephra north sector (Figure 9) in the earlier stages resulted
556 from coasts being sheltered from swells coming from the west and northwest by the
557 north-western part of the promontory. However, when the westernmost coasts were
558 reduced by marine erosion, these tephra coasts became more exposed and cliffs
559 retreated more rapidly (Figure 9). In addition, waves propagating from the west may

560 have transported sediments to the eastern edge of the promontory by long-shore
561 drift. They then protected the cliff from coastal erosion, slowing cliff retreat by ~77%.
562 However, as these eroded materials have smaller resisting force, they were quickly
563 removed by waves and the cliff retreat rate increased again (Figure 9). During the
564 visit to Capelinhos in 2017, a large landslide scar was observed in the north tephra
565 cliffs (Figure 10f). Slumping is probably the main mechanism of coastal retreat in
566 Capelinhos (Machado et al., 1962), whereby waves gradually remove materials from
567 the cliff base, leading to undermining and abrupt failure. Failure and swell action
568 then transport the fallen materials onto the foreshore.
569

570 4.4.2 Submarine

571 We have hypothesized that particles deposited at the shoreline may have
572 initially built a submarine slope (dashed brown line in profile B1 of Figure 6b) at the
573 angle of repose of 30° (Mitchell et al., 2000; Mitchell et al., 2012a). The inferred
574 platform edge in Figure 6b is everywhere seaward and shallower than this surface.
575 We estimate ~7×10^6 m^3 of sediments have been deposited in the uppermost slope to
576 prograde the platform edge based on the cross-sectional area between the 30°
577 surface (dashed brown line in Figure 6b) and modern slope, delimited by the inferred
578 platform edge and 1958 coastline.

579 We postulate the varied depth of the platform edge reflects cliff resisting force
580 (deeper edge where materials are less cohesive) and wave properties (deeper edge
581 exposed to taller and longer period waves, which affect the bed to greater depths).
582 For example, the lava south platform edge lies at only 30 m depth, which is
583 shallower than the tephra south platform edge at 50 m. However, the tephra north

584 platform edge at 40 m is shallower than the lava north platform edge at 45 m. On
585 average, the three northern platform edges at 50 m are slightly deeper than the
586 southern platform edges at 40 m.

587 The boulders imaged in Figure 7a immediately below the platform edge
588 presumably represent pyroclasts sourced from the eroding volcano flanks that spent
589 little time being rolled over the platform. Finer components were possibly
590 transported by storm-generated down-welling balance currents (Meireles et al.,
591 2013), contributing to the smooth seabed morphology below the platform edge.
592 Large rounded boulders in SCUBA dive images in Figure 7b and 7c at shallower
593 location S1 suggested they had been abraded in the surf zone for a while, although
594 their ages and lithologies are unclear. The clasts photographed during the nearshore
595 SCUBA dive at S2 (Figure 7d-7j) are more angular, implying a lack of abrasion and a
596 short transport distance from the nearby lava cliffs (Figure 10b).

597

598 4.5 Modelling of wave height attenuation

599 Figure 13a shows that increasing the width of a uniformly dipping platform of 3°
600 has little effect on wave heights arriving at the coastline. Similarly, varying the deep-
601 water wave height has little effect (Figure 13c). However, waves reaching the
602 coastlines vary greatly with platform dip (Figure 13b), as shallower dips imply a
603 greater distance travelled over shallower water and hence will be more attenuated.

604 In Figures 13d and 13g, we show how the attenuated wave height at the cliff
605 base declines rapidly with increasing platform width (to 100 m for uniform dip and 20
606 m for varying dip). Changes become more gradual when widths are > 100 m for
607 uniform dip and >20 m for varying dip and the conditions assumed. The cliff-incident

608 wave erosive F in Figures 13e and 13h was computed as described in section 3.5
609 using equation (12) and comprehensive strengths for lava cliffs of 51.6 MPa (section
610 4.1.2) and for tephra of 12 MPa (appendix 6). The different forms of the graphs in
611 Figures 13e and 13h from that in Figures 13d and 13g reveal the effect of the
612 threshold (F_R).

613 The model outputs for a platform with fixed dip are plotted logarithmically in
614 Figure 13f, so that we can see if wave erosive force follows an inverse power-law
615 similar to the coastline retreat rates in Figure 15. Although the independent variables
616 are different (platform width in Figure 13f and coastal retreat distance in Figure 15),
617 we might nevertheless expect to see similar patterns emerge if erosion rates are
618 proportional to erosive force (Sunamura et al., 2014). Differences between the two
619 curves in Figure 13f are due to the different coefficient k for breaking and broken
620 waves. The decline of $\log_{10}F$ with $\log_{10}W$ over the interval $\log_{10}W$ 0.8 to 1.4 (6 to 25
621 m) for breaking waves and $\log_{10}W$ 0.8 to 1.1 (6 to 13 m) for broken waves roughly
622 follows the trends in Figure 15b. However, this range of $\log_{10}W$ only corresponds to
623 platforms up to 25 m wide, not the major range of the data.

624 In Figure 13i for variably dipping platforms, the model for breaking waves
625 predicts $\log_{10}F$ declining from $\log_{10}W$ 0.8 to 2.5 (W = 6 to 316 m) somewhat like the
626 data in Figure 15b (comparing with those trends in aggregate, rather than individual
627 coastal sectors). The model for broken waves predicts $\log_{10}F$ declining from $\log_{10}W$
628 0.8 to 2.0 (W = 6 to 100 m) also somewhat like the data in Figure 15b. The model
629 gradients differ from the data trends for $\log_{10}W \geq 2.5$ ($W \geq 316$ m) for breaking
630 waves and for $\log_{10}W \geq 2.0$ ($W \geq 100$ m) for broken waves, but these parts of the
631 graphs are sensitive to cliff resistance, which is uncertain.

5. Discussion

Our results show that over the past six decades erosion has rapidly reduced the area of the Capelinhos cone to 17% of its original size but at rates that have dramatically decreased as the submarine platform left by erosion has widened. The geomorphology of the different sectors of the promontory varies, reflecting different post-eruptive development. Below, we discuss possible explanations for the varied coastline retreat rates between different lithologies and coastal orientations, as well as interpret the rapid decline in retreat rate with time. Finally, wider implications are considered for how rapidly Surtseyan cones and some analogous structures are eroded to form shallow banks.

5.1 Varied coastal erosion rates

Different cliff retreat rates and their changes over time may reflect varying intensity of wave effects (Trenhaile, 1987). The average of the Capelinhos coastal retreat rates briefly peaked at 164 m/yr (Table 1) for all sectors in the first half year of the post-eruptive development, but then rapidly decreased to 3%-17% of the peak value in the following decade, gradually slowing to 1-2 m/yr towards the time of our analysis. It is unclear exactly when erosion rates peaked, as that information would have required a more frequent monitoring in the earlier phase. The collapses of the early edifice reported by Machado et al. (1962) suggest erosion was concurrent with the eruption during which unmeasured amounts of material were being added as well as evacuating on to the island slope. Similar post-eruption changes were found in Surtsey (Romagnoli and Jakobsson, 2015), which may be explained by the following factors:

a) *Rock resistance.* In general, we expect loose tephra and thin and fractured

lava to be easily eroded, whereas well-bedded tephra layers containing lava chips and weakly jointed basaltic lava flows to have higher cliff resisting force. Similar varied resistance has been suggested previously for Surtsey (Jakobsson et al., 2000; Jakobsson et al., 2009; Romagnoli and Jakobsson, 2015). Lava cliffs with tephra bases were eroded rapidly, so the friability of the tephra clearly dominates the resistance of the entire cliff. On the whole, erosion occurs rapidly on cliffs formed with loose materials or with their base formed of them and gradually slows as more resistant material is exposed as found in the tephra south sector.

The Schmidt-hammer mean rebound value for the basalt blocks of 55 is typical of “strong rocks” according to the classification of Goudie (2006). For comparison, Schmidt hammer tests conducted on basalts from the Bodrum Peninsula (Turkey) produced rebound values of 35 to 55 (Dinçer et al., 2004) and tests on basalt cliffs on Lord Howe Island (SE Australia) yielded rebound values of 30 to 65, with the highest values associated with low joint density (Dickson et al., 2004).

In our study, we found some evidence for lower retreat rate for lava cliffs. For example, the north lava+tephra sector retreated more rapidly than the north lava sector in Figure 9. However, the tephra coast retreated more slowly. Nevertheless, we interpret these discrepancies as due to sediment dynamic effects as outlined earlier in section 4.4.1. Even if complicated by them, we anticipate some effect of cliff resistance to be present as in other sections.

b) *Local wave conditions.* Masselink et al. (2016) suggested the rate of morphologic evolution of coastlines is proportional to the frequency and height of extreme waves. The ERA models suggest upper 5-percentile wave heights of 4-12 m

682 (Figure 9) and periods of 11-16s in this site (Appendix 7b). However, the means of
683 these wave heights have increased by 3% and their associated period has increased
684 by 6% over the last six decades (Appendix 7), so it is unlikely the coastal retreat
685 rates have slowed because of declining wave impacts over time. Although there are
686 individual occurrences of rapid erosion coinciding with short-lived greater wave
687 heights in Figure 9 (e.g., tephra north from 17 to 22 years), there is no general
688 correlation between retreat rate and extreme wave height.
689
690 c) *Coastal orientation.* Coasts facing the strongest waves would be expected to
691 erode faster. This can explain the faster coastal retreat rates in the north and west
692 sectors (coastal sectors facing north and west in Figure 9). Refraction of shoaling
693 waves may also leave more obliquely oriented coasts affected by waves, leading to
694 their rapid erosion. Erosion has gradually modified coastal configuration through time
695 and left small headlands. Refraction of northwesterly swells may explain why the
696 southern Capelinhos coast (tephra and facing southwest) eroded nearly as rapidly as
697 the south lava coastline, which is more exposed to strong waves from northwest
698 (Figure 9). It was also affected by less frequent large swells from the SW.
699
700 d) *Changing wave exposure.* The northern tephra coast of Capelinhos was
701 initially sheltered from westerly waves (Figure 2l), perhaps explaining why it was the
702 slowest retreating coast in the first 20 years in Figure 9. The bay might also
703 represent a cul-de-sac for evacuating material. The tephra north sector subsequently
704 eroded more rapidly (Figure 9). Similarly, the lack of coastline retreat observed in
705 the northeast sandy beach of Surtsey from 1967-2007 (Romagnoli and Jakobsson,
706 2015) may be interpreted as the south part of the island protecting the northeast
707 sandy beach from exposure to west-southwest originating waves, which occurred

52% of the time. Other possible explanations include the leeside of the island accumulating sediments quarried and moved by longshore drift from the exposed side.

e) *Protection by eroded materials.* Our recent observations helped to verify the role of protection by eroded materials. In three locations, eroded materials deposited at the cliff base were found protecting the cliff from wave erosion. First, large angular lava boulders in southern Capelinhos (Figure 10b) were found armouring the cliff base. Second, protective talus formed by the failure of undermined high cliff was found in north Capelinhos (Figure 10e). The talus of hard blocks shields the friable pyroclasts as suggested elsewhere (Emery and Kuhn, 1982; Dickson, 2004). The amount of talus material that needs to be removed by waves after cliff collapses and before undermining resumes increases considerably as the cliff being dismantled grows taller around a conical edifice. This might also be a major factor slowing down the rate of coastal retreat. Third, a sandy beach (Figure 10f) emplaced by longshore sediment drift originating from the west protected the north Capelinhos tephra coast. The longshore shift itself disaggregated the loose materials, while the sandy beach forces waves to break and absorbs wave energy. Similarly, a palagonitized tephra cliff on Surtsey was found protected by lava boulder platforms/beaches built up by swash (Romagnoli and Jakobsson, 2015).

f) Tectonic movement: Romagnoli and Jakobsson (2015) suggested that tectonic subsidence of 1 m until 1991 caused by compaction of Surtsey affected the island's coastal retreat rates. Stephenson et al. (2017) suggested that a tectonic uplift of 1.01 m associated with the Kaikoura earthquake increased wave attenuation over a shore platform, consequently reducing coastal erosion rates there. At longer

734 time scales it has been shown that subsidence increases coastal retreat rates
735 (Quartau et al., 2018). Catalão et al. (2006) suggest that the Fajã sector of Faial
736 Island subsided by up to 1.5 m between 1937 and 1997 in relation to the Capelinhos
737 eruption, while the Capelinhos area itself is placed between the isoclines
738 representing 0 to 0.5 m subsidence. Although there are no vertical displacement
739 data for the Capelinhos promontory itself, metre-scale subsidence is possible for
740 reasons similar to Surtsey. We suggest that these reduced wave attenuation by only
741 a minor amount as the platform is much deeper than 1 m.
742

743 5.2 How the submarine platform evolved by wave erosion

744 We suggest that submarine platform developed in five phases (Figure 16).
745 Phase I: Capelinhos was shaped as a cone/promontory by a Surtseyan eruption with
746 its seaward flanks exposed to waves. Phase II: the post-eruptive wave erosion of the
747 coast created a submarine platform. Phase III: wave erosion progressively widened
748 and lowered the platform. Phase IV: a rugged surface covered with eroded boulders
749 was left by erosion. The eroded boulders on the platform surface were moved there
750 by the offshore sediment transport in response to storms (Scott et al., 2016; Burvingt
751 et al., 2017), perhaps moving to greater depths below the platform edge during more
752 violent storms (Rebelo et al., 2018). The platform edge may either represent the
753 edge of the original cone (Figure 16d), or it was extended by the deposition of
754 eroded materials (Figure 16e) as suggested by our analysis of the cross-sections in
755 Figure 6b. Phase V: in absence of further volcanism and mass wasting events,
756 continued wave erosion will eventually turn the promontory into a submerged bank
757 (Figure 16f).

758

759 5.3 The inverse power law relationship between coastal erosion rate and retreat
760 distance

761 The apparently simple inverse power-law relationship between rate of coastal
762 retreat R_r and retreat distance D (Figure 15b) stems partly from the increasing
763 attenuation of waves crossing the resulting submarine platform. The data for the
764 Surtsey coasts in Figure 15c (summarized in Table A3) suggest similar behaviours
765 for the lava, but not for tephra coasts. Deviations of retreat rate from the inverse
766 power law relationship can be caused by abrupt cliff collapses arising from
767 undercutting of cliffs by marine erosion.

768 Figure 15d shows that the square root of Sholan Island's area (approximately
769 coastal retreat distance) decreased nearly linearly with time after the end of its
770 eruption, implying a constant retreat rate in contrast to the later Capelinhos
771 evolution. The 15 m/yr average coastline retreat rate of Sholan Island (2012- 2017)
772 was much smaller than the earliest retreat rates of Capelinhos (56-326 m/yr) and
773 Surtsey (90-107.5 m/yr), reflecting the more moderate wave climate of the Red Sea.
774 The evolution of Sholan Island has been barely studied, so the lithology of the island
775 is poorly known. According to Xu et al. (2015) and Jónsson and Xu (2015), the
776 eruption failed to become effusive, so the edifice is probably mainly formed of
777 hydromagmatic/tephra deposits. The nearby islands of Rugged (located 1 km to the
778 south) and Haycock (3 km to the northeast) (Xu et al., 2015) may also partly shelter
779 Sholan Island from waves from northeast and south, while Capelinhos and Surtsey
780 are fully exposed. Moreover, the seasonal reversal of prevailing wave directions in
781 Red Sea allows Sholan Island to redeposit the loose materials eroded during
782 winter/spring in the north and in the south in summer (Xu et al., 2015). The linear
783 variation in Figure 15d suggests that wave attenuation was not significant during

784 these early stages of Sholan Island, as attenuation would be expected to reduce
785 erosion rate increasingly with time and make the graph non-linear.

786 Figure 14 shows predicted cliff-incident wave erosive force declining with
787 increasing platform width. As mentioned earlier, deposition at the platform edge may
788 have widened the platforms. However, extending the deeper part of the platform has
789 little effect on net attenuation (because it is deep) so we can still roughly compare
790 these model trends with platform width *W* with the erosion rates plotted against
791 coastline retreat distance *D*. In doing so, we acknowledge there is large uncertainty
792 in the resistance to erosion of the cliff materials, so the declines in *F* at large *W* are
793 not resolved realistically and differences between materials may not be so
794 significant.

795 The model predictions with varied platform dip in Figure 14 (lines C and D)
796 have somewhat similar gradients to the power-law trends in Figure 15b, but the
797 graphs for constant gradient platforms (lines A and B) mostly do not. Only lines A
798 and B in Figures 14a1 and 14a2 have acceptable graph gradients, but then only for
799 small *W*. Along the Tephra and Lava+Tephra coasts, it seems more likely that the
800 platform gradient varied. In other words, the platform was narrow initially, leading to
801 little wave attenuation and hence rapid erosion, but then deepened as it widened.
802 Wave attenuation was only important then in shallow water, hence leading to the
803 moderate decline in erosion rates. This is less clear for the lava cliffs as the predicted
804 erosive forces in both models are too low for erosion to occur.

805 Nevertheless, these inferences are speculative. We acknowledge that
806 discrepancies between the model predictions and the power law trends are partly
807 caused by the limitation of the numerical modelling that separately simulated erosive
808 force attacking cliff for breaking and broken waves, while types of waves attacking

809 cliffs (standing, breaking and broken) vary temporally depending on the cliff root
810 water level (Sunamura, 1992) . More importantly, the discrepancies could imply that
811 other factors are also important, in particular, the variation of cliff lithology, its joint
812 intensity (Kennedy, 2010) and consequently its cliff resisting force, along with the
813 temporary protection conferred by shelf deposits of eroded material (Figure 10b).
814

815 5.4 Development of shallow banks

816 The rapid decline found in Capelinhos may not be extended to all Surtseyan
817 cones if erosion rate depends so strongly on lithology, which is likely to vary.
818 However, the range of rates may be useful for suggesting the range of cone
819 longevity that may be possible. For example, the Costado da Nau (Figure 17a) is the
820 remnant of a previous Surtseyan eruption at Capelinhos (Waters and Fisher, 1971;
821 Camus et al., 1981), which occurred between 500 and 800 A.D. according to paleo-
822 magnetic data (Di Chiara et al., 2014). Waves removed most of the promontory
823 before the 1957/58 eruption when the Capelinhos cone was emplaced in front of the
824 Costado da Nau cliff, protecting it from further wave erosion. Monte da Guia located
825 in the SE of Faial Island (Figure 17a) is also a Surtseyan cone that has persisted for
826 longer（Madeira and Brum da Silveira, 2003）possibly partly because of wave
827 sheltering by the island and partly greater cliff resisting force (palagonitized tephra).

828 We can use our results to estimate how long it will take wave erosion to
829 remove the present Capelinhos promontory. In order to do this, we assume that
830 wave conditions will remain constant and that relative sea level will not change over
831 the next 100 yr significantly compared with the metre or so of vertical cliff interval
832 impacted by waves. Using the average power law relationship from Figure 15b and

833 solving for the edifice half-width by integration, the Capelinhos promontory will
834 become a submerged bank by 2118 A.D. This is later than the few decades
835 suggested by Cole et al. (2011).

836 Rapid wave erosion has turned some other Surtseyan cones in the Azores
837 into submerged banks more quickly than this. The features mentioned below are
838 located in Figure 17a. Sabrina Island reached a height of 90 m after its
839 emplacement in 1811 A.D. offshore NW São Miguel. The island stood above sea
840 level for 4 months (June to October, 1811) and is currently reduced to a bank lying
841 40 m below sea level (Moores and Fairbridge, 1997; Madeira and Brum da Silveira,
842 2003; Ramalho et al., 2013). NW of São Miguel, within the Terceira Rift, a larger
843 feature, the Dom João de Castro Seamount, erupted in 1720 A.D. forming a
844 subaerial cone that peaked at a maximum height of 250 m and disappeared after a
845 few months. Its top now lies at depths of 13 to 50 m (Santos et al., 2010). Many
846 other Surtseyan cones exist in the Azores but remain undated. One cone on
847 Princess Alice Bank now lies at 55 m depth (Figure 17b) and a littoral cone to the SE
848 of Pico now lies at 10-40 m depth (Mitchell et al., 2018). Several submerged banks
849 of wave erosion origin were also found on the shallow portions of Serreta Ridge and
850 SE of Angra do Heroísmo, lying between 30 and 180 m depth (Quartau et al., 2014).
851 A submerged bank lying at 80 m depth NW of Terceira Island originated from wave
852 erosion of two adjacent cones shown on Figure 17c.

853 These Azores submerged banks mainly lie between 10 and 55 m depth, with
854 one extreme at 180 m. The variation of their depths might be due to varying local
855 wave conditions and different ages, and hence different contemporary sea level,
856 though varied materials and hence resistance to erosion may also have played a

857 role. Modelling of changing wave propagation and its effect on cone erosion,
858 coupled with dating of samples, may help to resolve this issue.

859 Once submerged by erosion, the resulting shallow banks slow down waves in
860 comparison with adjacent deeper waters, leading to wave refraction and local wave
861 convergence over the banks. Hence, while the initial emergence of Surtseyan cones
862 above sea level inhibits the wave energy reaching the adjacent coasts, the
863 subsequently formed shallow bank may focus wave energy on the adjacent coastline
864 (the concave shape of the Costado da Nau coast previous to Capelinhos may have
865 been formed by this effect from the adjunct shallow platform around the two islets).
866 Consequently, dating shallow remnants of Surtseyan cones could turn out to be
867 useful for assessing how wave erosion has varied around adjacent coasts over time.

868

869 **6. Conclusions**

870 This study has characterised how rapidly the morphology of the coast and
871 near shore platforms have changed after the Surtseyan eruption of Capelinhos. The
872 average coastal retreat rate peaked at 164 m/yr in the first year after the eruption
873 and since then has quickly declined to 2 m/yr in the last decade. Coasts composed
874 of mixed lava and tephra and located in the northwest eroded most rapidly, explained
875 by the combined influences of weak rock, strong waves and orientation towards the
876 prevailing swells. Marine geophysical data revealed the rugged surface of the
877 submarine platform left behind by erosion. Seabed photos of the platform have
878 revealed large, angular and some rounded boulders on its surface. Marine erosion
879 has evidently lowered the platform as well as widened it.

The rate of coastal erosion varied as an inverse power law with retreat distance, representing a rapid decline in erosion with time. Wave attenuation contributed to this relationship. We find that the decline in wave erosive force predicted using a simple finite difference model most closely (though still only partially) reproduces the trend of the inverse power law if the platform started with a 30˚ gradient and gradually declined towards the present 3˚ gradient, rather than maintaining a constant gradient. However, other factors are also important, in particular, the varied cliff lithology and joint intensity, and consequently the cliff resisting force. Protection provided by eroded materials also complicates the interpretation.

Based on the observed inverse power law trend of erosion rates, we estimate that the promontory will eventually be submerged by 2118 A.D. Some other Surtseyan cones have eroded away more quickly than this, while the Monte da Guia has lasted much longer, so persistence in time varies strongly.

Acknowledgements

Gerd Masselink, at the University of Plymouth, Sigurjón Jónsson, at King Abdullah University of Science and Technology and Wayne Stephenson, at the University of Otago are kindly acknowledged for helpful discussions. Z.Z. thanks China Scholarship Council (CSC/201708060444) for financial support. The European Space Agency (ESA Project ID: 36098) is acknowledged for supplying earth observation data. The Significance of Modern and Ancient Submarine Slope Landslides (S4SLIDE) project (International Geoscience Programme (IGCP) -640) is acknowledged for a grant that permitted the presentation of this work in European

Geosciences Union General Assembly 2017. The open source software packages GMT (Wessel and Smith, 1991), GeoMapAPP (Ryan et al., 2009) and QGIS were used. Work at sea was supported by the Royal Society, the British Council (Germany), the Higher Education Funding Council for Wales, the Regional Directorate for Science and Technology of the Azores as well as projects GEMAS Project (funded by Regional Directorate for Environment of the Azores), MARINOVA (INTERREG IIIb—MAC/4.2/M11), MAROV (PDCTM/P/MAR/15249/1999) and MAYA (AdI/POSI/2003), OGAMP (INTERREG IIIb-MAC/4.2/A2 2001), MARMAC (INTERREG IIIb-03/MAC/4.2/A2 2004). Bathymetry data for Princess Alice Bank and Terceira Island were kindly shared by projects CORALFISH (FP7 ENV/2007/ 1/213144) and FAIVI (FP7/EUROFLEETS/228344) respectively. The authors acknowledge the crews of R/V *Arquipélago*, R/L *Águas Vivas*, R/V *Almirante Gago Coutinho*, R/V *L'Atalante* and R/L *Haliotis* and as well as the FAIVI cruise leader Francesco Chiocci. F.T. partially worked under a Ph.D. grant from the Fundação para a Ciência e a Tecnologia (FCT) ref. SFRH/BD/12885/2003. R.Q. acknowledges his IF/00635/2015 research contract funded by FCT. MARE is also supported by FCT through the strategic project UID/MAR/04292/2013. CARIS HIPS and SIPS from Caris Inc. was used under the academic agreement with IMAR-Instituto do Mar ref. 2009-02- APP08. Finally, we thank the constructive and helpful comments by the editor, Claudia Romagnoli and an anonymous reviewer.

924 **References:**

925 Andrade, C., R. Trigo, M. Freitas, M. Gallego, P. Borges, and A. Ramos. 2008. Comparing
926 historic records of storm frequency and the North Atlantic Oscillation (NAO)
927 chronology for the Azores region. *The Holocene* 18 (5):745-754,
928 doi:10.1177/0959683608091794.
929 Arthur, R. S. 1951. The effect of islands on surface waves. *Bulletin of the Scripps Institution*
930 *of Oceanography*.University of California Press, Berkeley and Los Angeles, 24p.
931 Borges, P. 2004. Ambientes litorais nos grupos Central e Oriental do arquipélago dos
932 Açores, conteúdos e dinâmica de microescala. Ponta Delgada, Portugal:
933 Universidade dos Açores, Ph. D. thesis, 413p.
934 Burvingt, O., Masselink, G., Russell, P. and Scott, T., 2017. Classification of beach response
935 to extreme storms. *Geomorphology*, *295*, pp.722-737, doi:
936 10.1016/j.geomorph.2017.07.022.
937 Caires, S., and Sterl, A., 2003, Validation of ocean wind and wave data using triple
938 collocation: *J. Geophys. Res*., v. 108, p. Paper C3098, doi:3010.1029/2002JC001491.
939 Camus, G., P. Boivin, A. D. G. De Herve, A. Gourgaud, G. Kieffer, J. Mergoil, and P. Vincent.
940 1981. Le Capelinhos (Faïal, Açores) vingt ans après son éruption: le modèle éruptif
941 «Surtseyen» et les anneaux de tufs hyaloclastiques. *Bulletin Volcanologique* 44
942 (1):31-42, doi:10.1007/bf02598187.
943 Carvalho, F. 2003. Elementos do clima de agitação marítima no grupo central dos Açores.
944 *Instituto de Meteorologia, Lisboa*.97p.
945 Catalão, J., J. Miranda, and N. Lourenço. 2006. Deformation associated with the Faial
946 (Capelinhos) 1957–1958 eruption: Inferences from 1937–1997 geodetic
947 measurements. *Journal of Volcanology and Geothermal Research* 155 (3):151-163,
948 doi:10.1016/j.jvolgeores.2006.03.028.
949 Cole, P., A. Duncan, and J. Guest. 1996. The rise and fall of Capelinhos volcano, on Faial, in
950 the Azores. *Geology Today* 12:68-72, doi:10.1046/j.1365-2451.1996.00010.x.

951 Cole, P., J. Guest, A. Duncan, and J.-M. Pacheco. 2001. Capelinhos 1957–1958, Faial,
952 Azores: deposits formed by an emergent surtseyan eruption. *Bulletin of Volcanology*
953 63 (2-3):204-220, doi:10.1007/s004450100136.
954 Dee, D. P., S. Uppala, A. Simmons, P. Berrisford, P. Poli, S. Kobayashi, U. Andrae, M.
955 Balmaseda, G. Balsamo, and P. Bauer. 2011. The ERA-Interim reanalysis:
956 Configuration and performance of the data assimilation system. *Quarterly Journal of*
957 *the royal meteorological society* 137 (656):553-597, doi:10.1002/qj.828.
958 Di Chiara, A., F. Speranza, M. Porreca, A. Pimentel, F. D. A. Caracciolo, and J. Pacheco.
959 2014. Constraining chronology and time-space evolution of Holocene volcanic
960 activity on the Capelo Peninsula (Faial Island, Azores): The paleomagnetic
961 contribution. *Geological Society of America Bulletin* 126 (9-10):1164-1180,
962 doi:10.1130/b30933.1.
963 Dickson, M., D. Kennedy, and C. Woodroffe. 2004. The influence of rock resistance on
964 coastal morphology around Lord Howe Island, southwest Pacific. *Earth Surface*
965 *Processes and Landforms* 29 (5):629-643, doi:10.1002/esp.1119.
966 Dickson, M. 2004. The development of talus slopes around Lord Howe island and
967 implications for the history of island planation. *Australian Geographer* 35 (2):223-238,
968 doi:10.1080/0004918042000249520.
969 Dinçer, I., A. Acar, I. Çobanoğlu, and Y. Uras. 2004. Correlation between Schmidt hardness,
970 uniaxial compressive strength and Young's modulus for andesites, basalts and tuffs.
971 *Bulletin of Engineering Geology and the Environment* 63 (2):141-148,
972 doi:10.1007/s10064-004-0230-0.
973 Emery, K., and G. Kuhn. 1982. Sea cliffs: their processes, profiles, and classification.
974 *Geological Society of America Bulletin* 93 (7):644-654, doi: 10.1130/0016-
975 7606(1982)93<644:SCTPPA>2.0.CO;2.

976 Farrell, E. J., H. Granja, L. Cappietti, J. T. Ellis, B. Li, and D. J. Sherman. 2009. Wave
977 transformation across a rock platform, Belinho, Portugal. *Journal of Coastal*
978 *Research*:44-48, doi:10.2112/jcoastres-d-12-00166.1.
979 Forjaz, V. H. 2007. Vulcão dos Capelinhos: memórias 1957-2007: Observatório
980 Vulcanológico e Geotérmico dos Açores. 826p.
981 Forjaz, V. H., Z. França, J. Tavares, L. Almeida, and J. Rodrigues. 2010. Dos vulcões dos
982 Açores− From the Azores vulcanoes: Ponta Delgada: Publiçor. 169p.
983 Goudie, A. S. 2006. The Schmidt Hammer in geomorphological research. *Progress in*
984 *Physical Geography* 30 (6):703-718, doi:10.1177/0309133306071954.
985 InstitutoGeográficodoExército. 2001. Portuguese military map, sheet 4, Praia do Norte
986 (Faial-Acores), scale 1:25,0000, Lisboa.
987 Jakobsson, S., K. Thors, Á. Vésteinsson, and L. Ásbjörnsdóttir. 2009. Some aspects of the
988 seafloor morphology at Surtsey volcano: The new multibeam bathymetric survey of
989 2007. *Surtsey Res* 12:9-20.
990 Jakobsson, S. P., G. Gudmundsson, and J. G. Moore. 2000. Geological monitoring of
991 Surtsey, Iceland, 1967–1998. *Surtsey Res* 11:99-108.
992 Jónsson, S., & Xu, W. (2015). Volcanic eruptions in the southern Red Sea during 2007–2013.
993 In *The Red Sea* (pp. 175-186). Springer, Berlin, Heidelberg.
994 Kahraman, S., 2001. A correlation between P-wave velocity, number of joints and Schmidt
995 hammer rebound number. International Journal of Rock Mechanics and Mining
996 Sciences, 38(5), pp.729-733.
997 Kennedy, D.M., 2010. Geological control on the morphology of estuarine shore platforms:
998 Middle Harbour, Sydney, Australia. *Geomorphology*, 114(1-2), pp.71-77,
999 doi:10.1016/j.geomorph.2009.02.012.
1000 Kokelaar, B. 1983. The mechanism of Surtseyan volcanism. *Journal of the Geological*
1001 *Society* 140 (6):939-944, doi:10.1144/gsjgs.140.6.0939.

1002 Kokelaar, B. P., and G. P. Durant. 1983. The submarine eruption and erosion of Surtla
1003 (Surtsey), Iceland. *Journal of Volcanology and Geothermal Research* 19 (3-4):239-
1004 246, doi:10.1016/0377-0273(83)90112-9.
1005 Lee, H. S. 2014. Modelling extreme sea levels due to sea level rise and storm surge in the
1006 Seto Inland Sea, Japan. *Coastal Engineering Proceedings* 1 (34):1,
1007 doi:10.9753/icce.v34.management.1.
1008 Ma, B., Wu, S., Betzler, C., Qin, Z., Mi, L., Gao, W., Bai, H., Wu, F. and Dong, D., 2018.
1009 Geometry, internal architecture, and evolution of buried volcanic mounds in the
1010 northern South China Sea. *Marine and Petroleum Geology*, 97, pp.540-555, DOI:
1011 10.1016/j.marpetgeo.2018.07.029.
1012 Machado, F., J. Nascimento, and A. Denis. 1959. Evolução topográfica do cone vulcânico
1013 dos Capelinhos. *Serv Geol Port Mere* 4:65-67,
1014 Machado, F., W. H. Parsons, A. F. Richards, and J. W. Mulford. 1962. Capelinhos eruption
1015 of Fayal volcano, Azores, 1957–1958. *Journal of Geophysical Research* 67 (9):3519-
1016 3529, doi:10.1029/jz067i009p03519.
1017 Machado, F., and T. Freire. 1985. Cone dos Capelinhos em 1981: *Açoreana* 6: 261-266.
1018 Madeira, J., and A. Brum da Silveira. 2003. Active tectonics and first paleoseismological
1019 results in Faial, Pico and S. Jorge islands (Azores, Portugal). *Annals of Geophys.*
1020 46:733-761.
1021 Madeira, J., A. B. da Silveira, A. Hipólito, and R. Carmo. 2015. Active tectonics in the central
1022 and eastern Azores islands along the Eurasia–Nubia boundary: a review. *Geological*
1023 *Society, London, Memoirs* 44 (1):15-32, doi:10.1144/M44.3.
1024 Madin, J. S., K. P. Black, and S. R. Connolly. 2006. Scaling water motion on coral reefs:
1025 from regional to organismal scales. *Coral Reefs* 25 (4):635-644, doi:10.1007/s00338-
1026 006-0137-2.
1027 Masselink, G., T. Scott, T. Poate, P. Russell, M. Davidson, and D. Conley. 2016. The
1028 extreme 2013/2014 winter storms: hydrodynamic forcing and coastal response along

1029 the southwest coast of England. *Earth Surface Processes and Landforms* 41 (3):378-
1030 391, doi:10.1002/esp.3836.
1031 McCall, R., G. Masselink, M. Austin, T. Poate, and T. Jager. 2017. Modelling incident-band
1032 and infragravity wave dynamics on rocky shore platforms. *Coastal Dynamics* Paper
1033 No. 144.
1034 Meireles, R. P., R. Quartau, R. S. Ramalho, A. C. Rebelo, J. Madeira, V. Zanon, and S. P.
1035 Ávila. 2013. Depositional processes on oceanic island shelves–Evidence from storm-
1036 generated Neogene deposits from the mid-North Atlantic. *Sedimentology* 60
1037 (7):1769-1785, doi:10.1111/sed.12055.
1038 Melo, C.S., Ramalho, R.S., Quartau, R., Hipólito, A., Gil, A., Borges, P.A., Cardigos, F., Ávila,
1039 S.P., Madeira, J. and Gaspar, J.L., 2018. Genesis and morphological evolution of
1040 coastal talus-platforms (fajãs) with lagoons: The case study of the newly-formed Fajã
1041 dos Milagres (Corvo Island, Azores). *Geomorphology*, *310*, pp.138-152, doi:
1042 10.1016/j.geomorph.2018.03.006.
1043 Mitchell, N.C., Tivey, M.A. and Gente, P., 2000. Seafloor slopes at mid-ocean ridges from
1044 submersible observations and implications for interpreting geology from seafloor
1045 topography. *Earth and Planetary Science Letters*, 183(3-4), pp.543-555, doi:
1046 10.1016/S0012-821X(00)00270-3.
1047 Mitchell, N. C., C. Beier, P. Rosin, R. Quartau, and F. Tempera. 2008. Lava penetrating
1048 water: Submarine lava flows around the coasts of Pico Island, Azores. *Geochem.*
1049 *Geophys. Geosyst.* 9:Paper Q03024, doi:03010.01029/02007GC001725.
1050 Mitchell, N.C., Quartau, R. and Madeira, J., 2012a. Assessing landslide movements in volcanic
1051 islands using near-shore marine geophysical data: south Pico island, Azores. *Bulletin of*
1052 *Volcanology*, 74(2), pp.483-496, doi: 10.1007/s00445-011-0541-5.
1053 Mitchell, N. C., Masselink, G., Huthnance, J. M., Fernández-Salas, L. M., and Lobo, F. J., 2012b,
1054 Depths of modern coastal clinoforms: *J. Sed. Res*., v. 82, p. 469-481,
1055 doi:10.2110/jsr.2012.40.

1056 Mitchell, N. C., Stretch, R., Tempera, F., and Ligi, M., 2018, Volcanism in the Azores: A
1057 Marine Geophysical Perspective. In: U. Kueppers & C. Beier (Eds.), Volcanoes of the
1058 Azores. Springer series “Active volcanoes”, 458P, doi: 10.1007/978-3-642-32226-6.
1059 Moore, J. G. 1985. Structure and eruptive mechanisms at Surtsey Volcano, Iceland. *Geol.*
1060 *Mag.* 122:649-661, doi:10.1017/s0016756800032052.
1061 Moores, E. M., and R. W. Fairbridge. 1997. *Encyclopedia of European and Asian regional*
1062 *geology*: Springer Science & Business Media. Springer Netherlands.804p.
1063 Murtagh, R. M., and J. D. White. 2013. Pyroclast characteristics of a subaqueous to
1064 emergent Surtseyan eruption, Black Point volcano, California. *Journal of Volcanology*
1065 *and Geothermal Research* 267:75-91, doi:10.1016/j.jvolgeores.2013.08.015.
1066 Ogawa, H., P. Kench, and M. Dickson. 2012. Field Measurements of Wave Characteristics
1067 on a Near-Horizontal Shore Platform, Mahia Peninsula, North Island, New Zealand.
1068 *Geographical Research* 50 (2):179-192, doi:10.1111/j.1745-5871.2011.00715.x.
1069 Poate, T., G. Masselink, M. Austin, M. Dickson, and P. Kench. 2016. Observation of Wave
1070 Transformation on Macro-tidal Rocky Platforms. *Journal of Coastal Research* 75
1071 (sp1):602-606, doi:10.2112/si75-121.1.
1072 Poate, T., G. Masselink, M. J. Austin, M. Dickson, and R. McCall. 2017. The role of bed
1073 roughness in wave transformation across sloping rock shore platforms. *Journal of*
1074 *Geophysical Research: Earth Surface*. doi: 10.1002/2017JF004277.
1075 Ponce de León, S., and C. Guedes Soares. 2005. On the sheltering effect of islands in
1076 ocean wave models. *Journal of Geophysical Research: Oceans* 110 (C9),
1077 doi:10.1029/2004jc002682.
1078 QGIS Development Team, 2016. QGIS Geographic Information System. Open Source
1079 Geospatial Foundation. URL http://qgis.org.
1080 Quartau, R., A. Hipólito, C. Romagnoli, D. Casalbore, J. Madeira, F. Tempera, C. Roque,
1081 and F. Chiocci. 2014. The morphology of insular shelves as a key for understanding
1082 the geological evolution of volcanic islands: Insights from Terceira Island (Azores).

Geochemistry, Geophysics, Geosystems 15 (5):1801-1826, doi:10.1002/2014gc005248.

Quartau, R., F. Tempera, N. C. Mitchell, L. M. Pinheiro, H. Duarte, P. O. Brito, C. Bates, and J. H. Monteiro. 2012. Morphology of the Faial Island shelf (Azores): The interplay between volcanic, erosional, depositional, tectonic and mass-wasting processes. *Geochemistry, Geophysics, Geosystems* 13 (4), doi:10.1029/2011gc003987.

Quartau, R., A. S. Trenhaile, N. C. Mitchell, and F. Tempera. 2010. Development of volcanic insular shelves: Insights from observations and modelling of Faial Island in the Azores Archipelago. *Marine Geology* 275:66-83, doi:10.1016/j.margeo.2010.04.008.

Quartau, R. 2007. The insular shelf of Faial: morfological and sedimentary evolution. Dep. de Geociências. Univ. de Aveiro. Aveiro, Portugal. Ph.D. thesis, 301p.

Quartau, R., Trenhaile, A.S., Ramalho, R.S., Mitchell, N.C., 2018. The role of subsidence in shelf widening around ocean island volcanoes: Insights from observed morphology and modeling. Earth and Planetary Science Letters 498, 408-417.

Ramalho, R. S., R. Quartau, A. S. Trenhaile, N. C. Mitchell, C. D. Woodroffe, and S. P. Ávila. 2013. Coastal evolution on volcanic oceanic islands: A complex interplay between volcanism, erosion, sedimentation, sea-level change and biogenic production. *Earth-Science Reviews* 127:140-170, doi:10.1016/j.earscirev.2013.10.007.

Rebelo, A.C., Johnson, M.E., Quartau, R., Rasser, M.W., Melo, C.S., Neto, A.I., Tempera, F., Madeira, P. and Ávila, S.P., 2018. Modern rhodoliths from the insular shelf of Pico in the Azores (Northeast Atlantic Ocean). *Estuarine, Coastal and Shelf Science*, doi: 10.1016/j.ecss.2018.05.029.

Romagnoli, C., and S. Jakobsson. 2015. Post-eruptive morphological evolution of island volcanoes: Surtsey as a modern case study. *Geomorphology* 250:384-396, doi:10.1016/j.geomorph.2015.09.016.

1108 Romer, R.H.W., Beier, C., Haase, K.M. and Hübscher, C., 2018. Correlated changes
1109 between volcanic structures and magma composition in the Faial volcanic system,
1110 Azores. *Frontiers in Earth Science*, *6*, p.78, doi: 10.3389/feart.2018.00078.
1111 Rusu, L., and C. G. Soares. 2012. Wave energy assessments in the Azores islands.
1112 *Renewable Energy* 45:183-196, doi:10.1016/j.renene.2012.02.027.
1113 Ryan, W. B. F., S. M. Carbotte, J. O. Coplan, S. O'Hara, A. Melkonian, R. Arko, R. A.
1114 Wiessel, V. Ferrini, A. Goodwillie, F. Nitsche, J. Bonczkowski, and R. Zemsky. 2009.
1115 Global multi-resolution topography synthesis. *Geochem. Geophys. Geosys*. 10:Paper
1116 Q03014, doi:10.1029/2008gc002332.
1117 Santos, Â., Mendes, S. and Corte-Real, J., 2014. Impacto da tempestade Hercules, em
1118 Portugal. *Finisterra-Revista Portuguesa de Geografia*, (98), pp.197-220.
1119 Santos, R. S., F. Tempera, A. Colaço, F. Cardigos, and T. Morato. 2010. Dom João de
1120 Castro Seamount. *Oceanography* 23:200-201, doi:10.5670/oceanog.2010.83.
1121 Saptono, S., Kramadibrata, S. and Sulistianto, B., 2013. Using the Schmidt hammer on rock
1122 mass characteristic in sedimentary rock at tutupan coal mine. *Procedia Earth and*
1123 *Planetary Science*, *6*, pp.390-395, doi: 10.1016/j.proeps.2013.01.051.
1124 Scott, T., Masselink, G., O'Hare, T., Saulter, A., Poate, T., Russell, P., Davidson, M. and
1125 Conley, D., 2016. The extreme 2013/2014 winter storms: Beach recovery along the
1126 southwest coast of England. *Marine Geology*, *382*, pp.224-241, doi:
1127 10.1016/j.margeo.2016.10.011.
1128 Short, A. D. 1996. The role of wave height, period, slope, tide range and embaymentisation
1129 in beach classifications: a review. *Revista Chilena de Historia Natural* 69 (4):589-604.
1130 Stephenson, W.J., Dickson, M.E. and Denys, P.H., 2017. New insights on the relative
1131 contributions of coastal processes and tectonics to shore platform development
1132 following the Kaikōura earthquake. *Earth Surface Processes and Landforms*, *42*(13),
1133 pp.2214-2220, doi: 10.1002/esp.4176.

1134 Sterl, A., and S. Caires. 2005. Climatology, variability and extrema of ocean waves: The
1135 web-based KNMI/ERA-40 wave atlas. *Int. J. Climatol*. 25:963-977,
1136 doi:10.1002/joc.1175.
1137 Sunamura, T. 1977. A relationship between wave-induced cliff erosion and erosive force of
1138 waves. *The Journal of Geology* 85 (5):613-618, doi:10.1086/628340.
1139 Sunamura, T. 1992. Geomorphology of rocky coasts. edited by E. C. F. Bird. Vol. 302. New
1140 York: John Wiley.302p, doi:10.7202/033013ar.
1141 Sunamura, T., H. Tsujimoto, and H. Aoki. 2014. The rock coast of Japan. *Geological Society,*
1142 *London, Memoirs* 40 (1):203-223, doi:10.1144/m40.12.
1143 Tank, A. M. G. K., F. W. Zwiers, and X. Zhang. 2009. Guidelines on analysis of extremes in
1144 a changing climate in support of informed decisions for adaptation. *World*
1145 *Meteorological Organization*. 52p.
1146 Tempera, F. 2008. Benthic habitats of the extended Faial Island shelf and their relationship
1147 to geologic, oceanographic and infralittoral biological features. University of St
1148 Andrews, St Andrews, UK. Ph.D. thesis, 341p.
1149 Thorarinsson, S. 1967. The Surtsey eruption and related scientific work. *Polar Record* 13
1150 (86):571-578, doi:10.1017/s0032247400058113.
1151 Thorarinsson, S. 1968. The Surtsey eruption: Course of events during the year 1967.
1152 *Surtsey Res Prog Rep* 4:143-148.
1153 Trenhaile, A. S. 1987. *The geomorphology of rock coasts*: Oxford University Press,
1154 USA.384p.
1155 Trenhaile, A. S. 2000. Modeling the development of wave-cut shore platforms. *Mar. Geol.*
1156 166:163-178, doi:10.1016/s0025-3227(00)00013-x.
1157 Uppala, S. M., P. Kållberg, A. Simmons, U. Andrae, V. d. Bechtold, M. Fiorino, J. Gibson, J.
1158 Haseler, A. Hernandez, and G. Kelly. 2005. The ERA-40 re-analysis. *Quarterly*
1159 *Journal of the royal meteorological society* 131 (612):2961-3012,
1160 doi:10.1256/qj.04.176.

1161 Waters, A. C., and R. V. Fisher. 1971. Base surges and their deposits: Capelinhos and Taal
1162 volcanoes. *Journal of Geophysical Research* 76 (23):5596-5614,
1163 doi:10.1029/jb076i023p05596.
1164 Wessel, P., and W. H. F. Smith. 1991. Free software helps map and display data. Eos,
1165 Transactions, *American Geophysical Union* 72:441, doi:10.1029/90eo00319.
1166 White, J. D. 1996. Pre-emergent construction of a lacustrine basaltic volcano, Pahvant Butte,
1167 Utah (USA). *Bulletin of Volcanology* 58 (4):249-262, doi:10.1007/s004450050138.
1168 Whittaker, R. J. 1998. Island biogeography. Oxford: Oxford University Press. 285p.
1169 Xu, W., J. Ruch, and S. Jónsson. 2015. Birth of two volcanic islands in the southern Red
1170 Sea. *Nature communications* 6, doi: 10.1038/ncomms8104.

Figures:

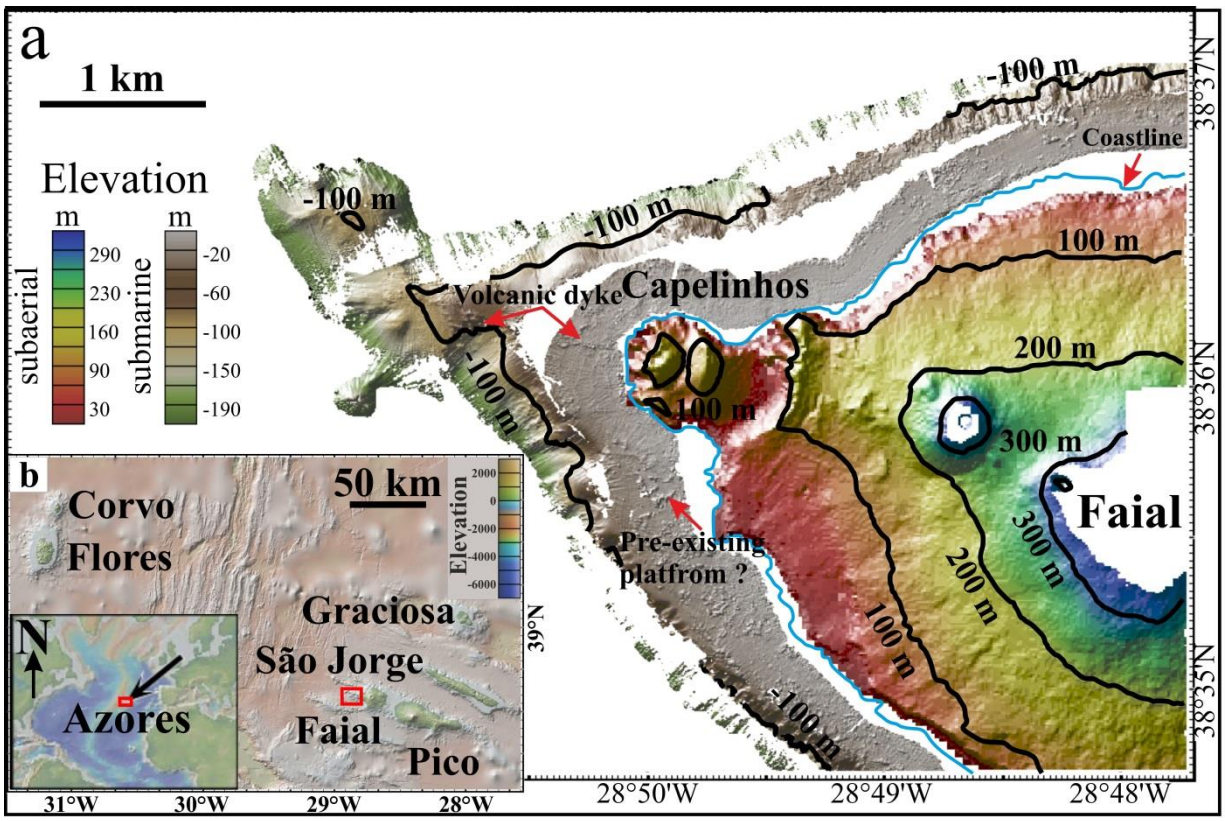

Figure 1. (a) Morphology of the Capelinhos promontory. Onshore topography and multibeam bathymetry are shown illuminated from the north. Topography is from Instituto Geográfico do Exército (2001). Bathymetry is from Mitchell et al. (2008) and Tempera (2008). (b) Location of panel (a) (red box) overlain on a map produced using GeoMapApp (Ryan et al., 2009).

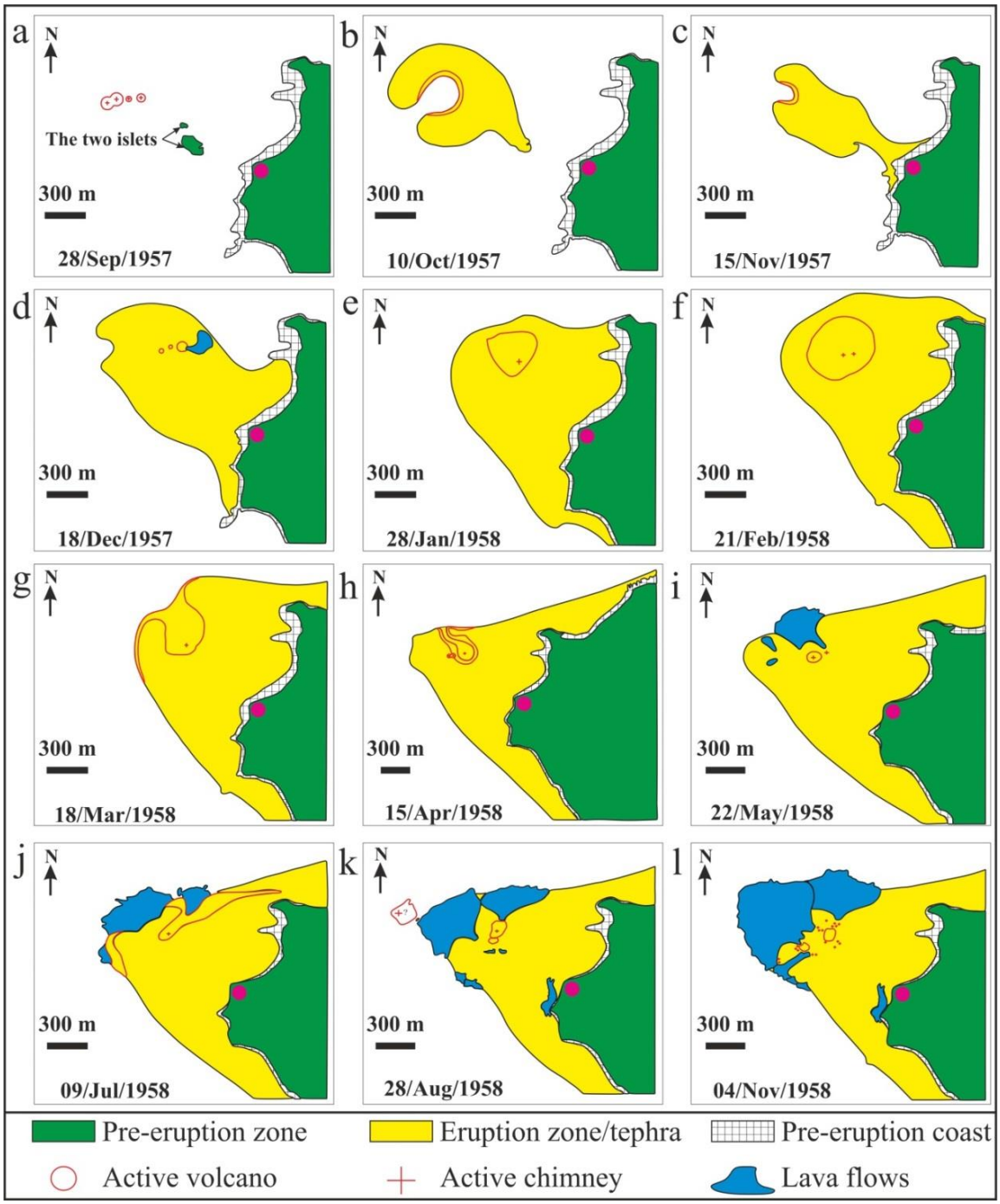

Figure 2. Physiographic and lithologic evolution of Capelinhos promontory from the initial eruption (September 1957) to the end of the eruption (November 1958) adapted from Machado et al. (1959). Pink circle locates the Capelinhos lighthouse.

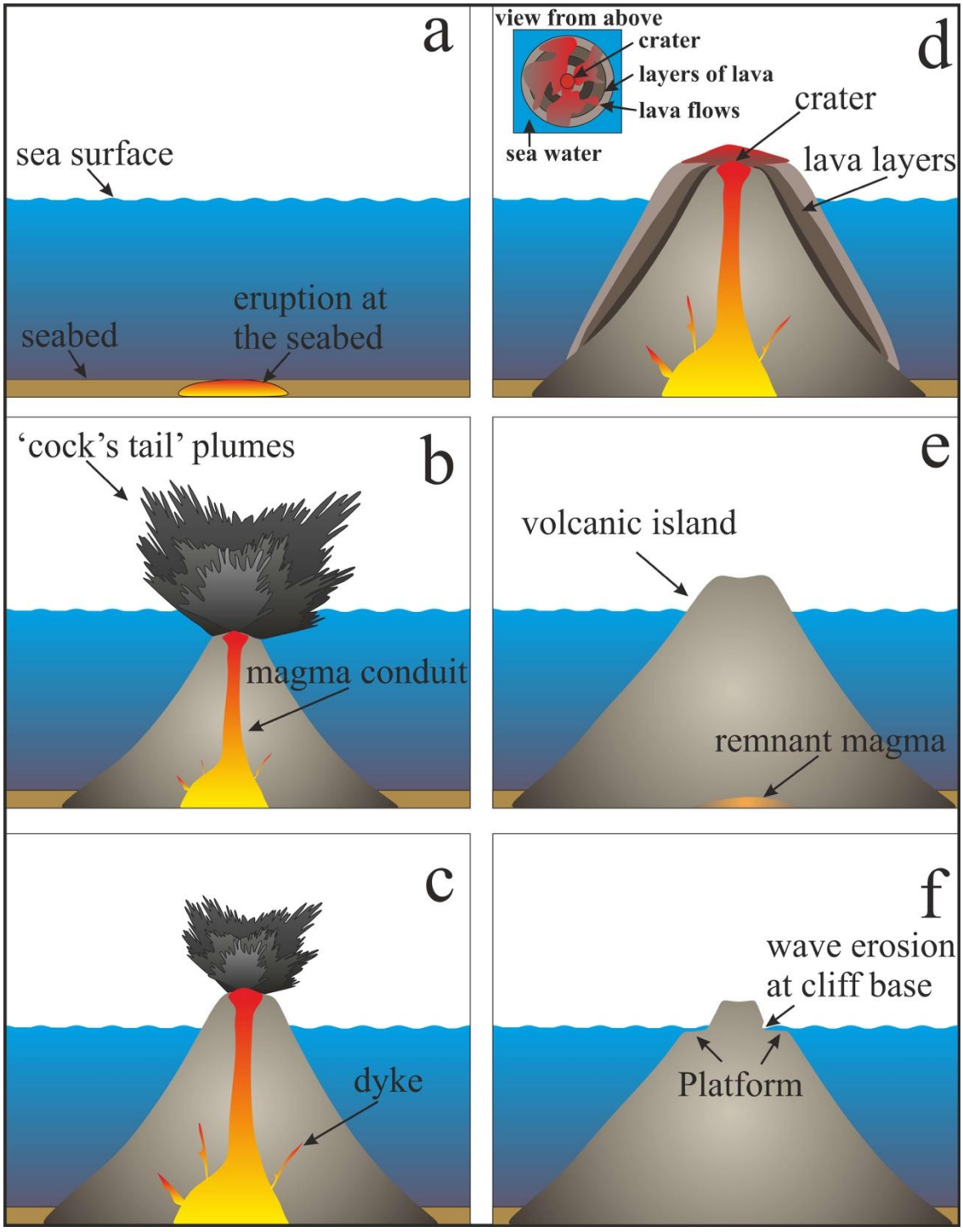

1183 Figure 3. Stages by which Surtseyan eruptions form volcanic islands, based
1184 on work of Moore (1985). (a) Initial eruption of magma at the seafloor. (b)
1185 Violent submarine eruption project characteristic "cock's tail" plumes of gas,
1186 steam and black tephra subaerially. (c) A cinder ring forms above sea level

from volcanic ashes and other tephra. (d) Cinder ring prevents seawater from entering the vent. Consequently, lava extrudes less violently, eventually with flows topping previous tephra layers. (e) Volcanic activity gradually ceases and magma conduit cools down. (f) Volcanic activity stops, leaving the edifice to evolve purely from erosion and sediment transport. Submarine platform develops on the flanks under the effect of wave erosion.

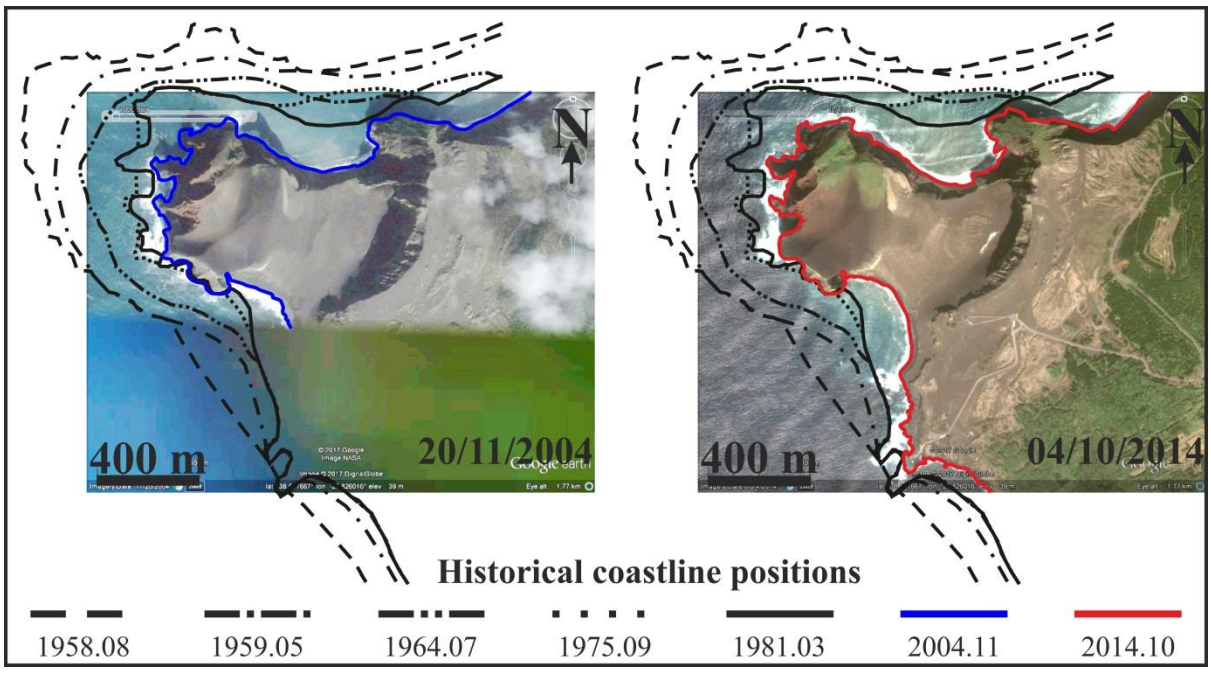

Figure 4. Coastline positions in 2004 and 2014 from Google Earth images (google.com) and previously reported historical positions from Machado and Freire (1985). The length of marked coastline in 2014 was 5079 m (marked in red). The coastline of 2004 (marked in blue) is incomplete due to lack of Google Earth images in the south.

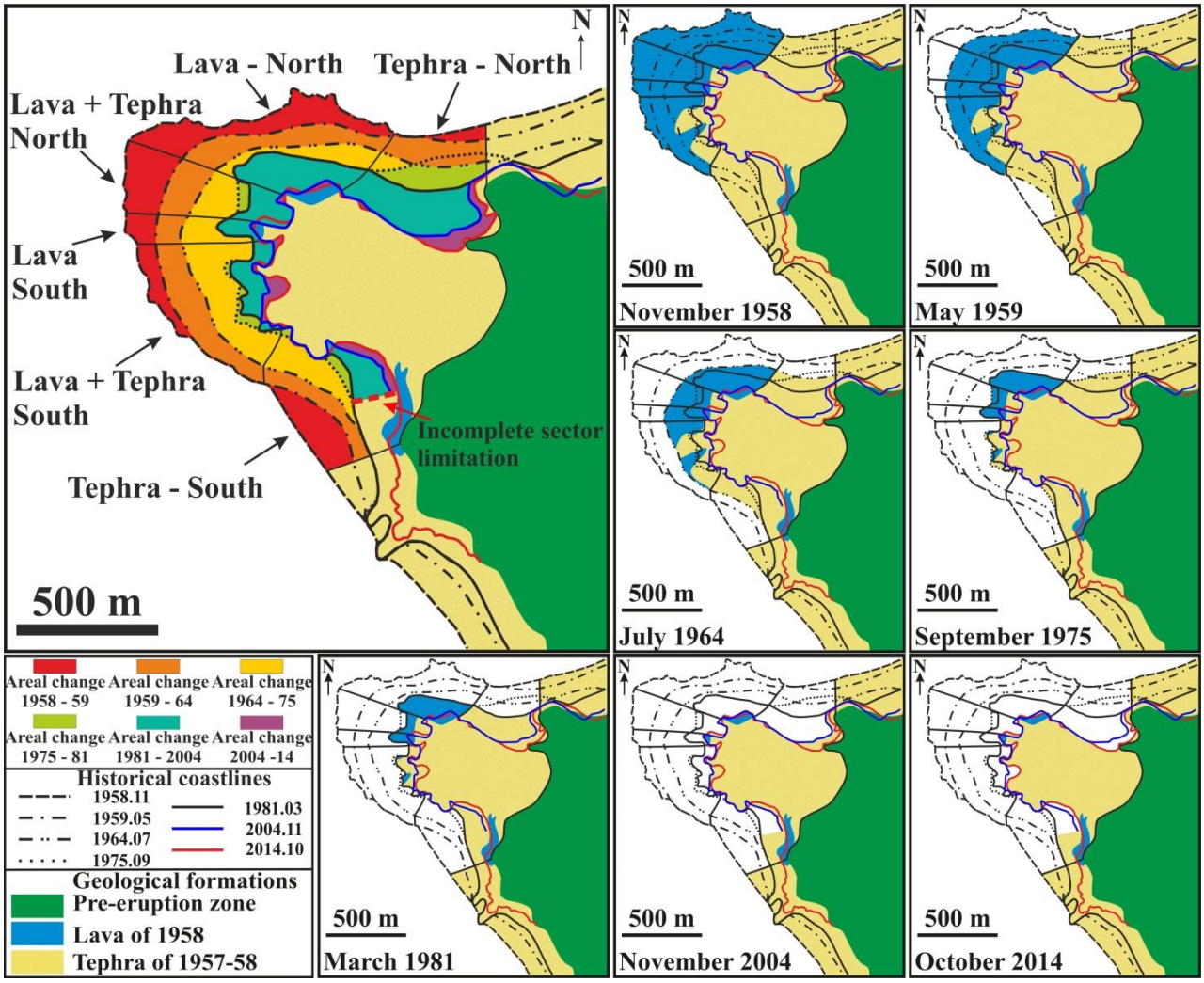

Figure 5. Evolution of Capelinhos based on coastlines of Figure 4.Six sectors were classified based on their different locations (north or south) and lithologies (lava, tephra and mixed lava and tephra). The red dashed line locates the incomplete coastline in the tephra south sector due to lack of data.

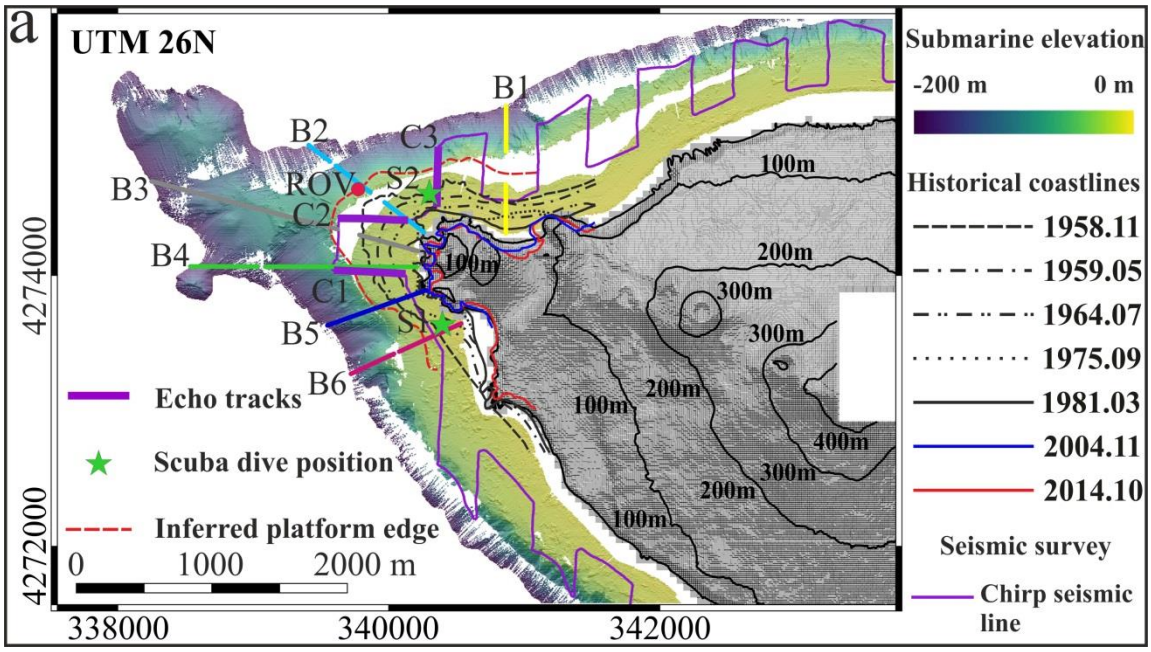

1206

1207 Figure 6. Profiles used to analyse the morphology of the platform. (a)
1208 Locations of the six cross-sections in (b) and three Chirp profiles in (c). Red
1209 circle and green stars locate respectively the underwater photographs taken
1210 by ROV and SCUBA divers shown in Figure 7. Submarine bathymetry and
1211 subaerial elevation data are illuminated from the north using GeoMapApp
1212 (Ryan et al., 2009). Elevations are contoured every 100 m. Coordinates are
1213 in Universal Transverse Mercator (UTM) projection metres (zone 26 N).

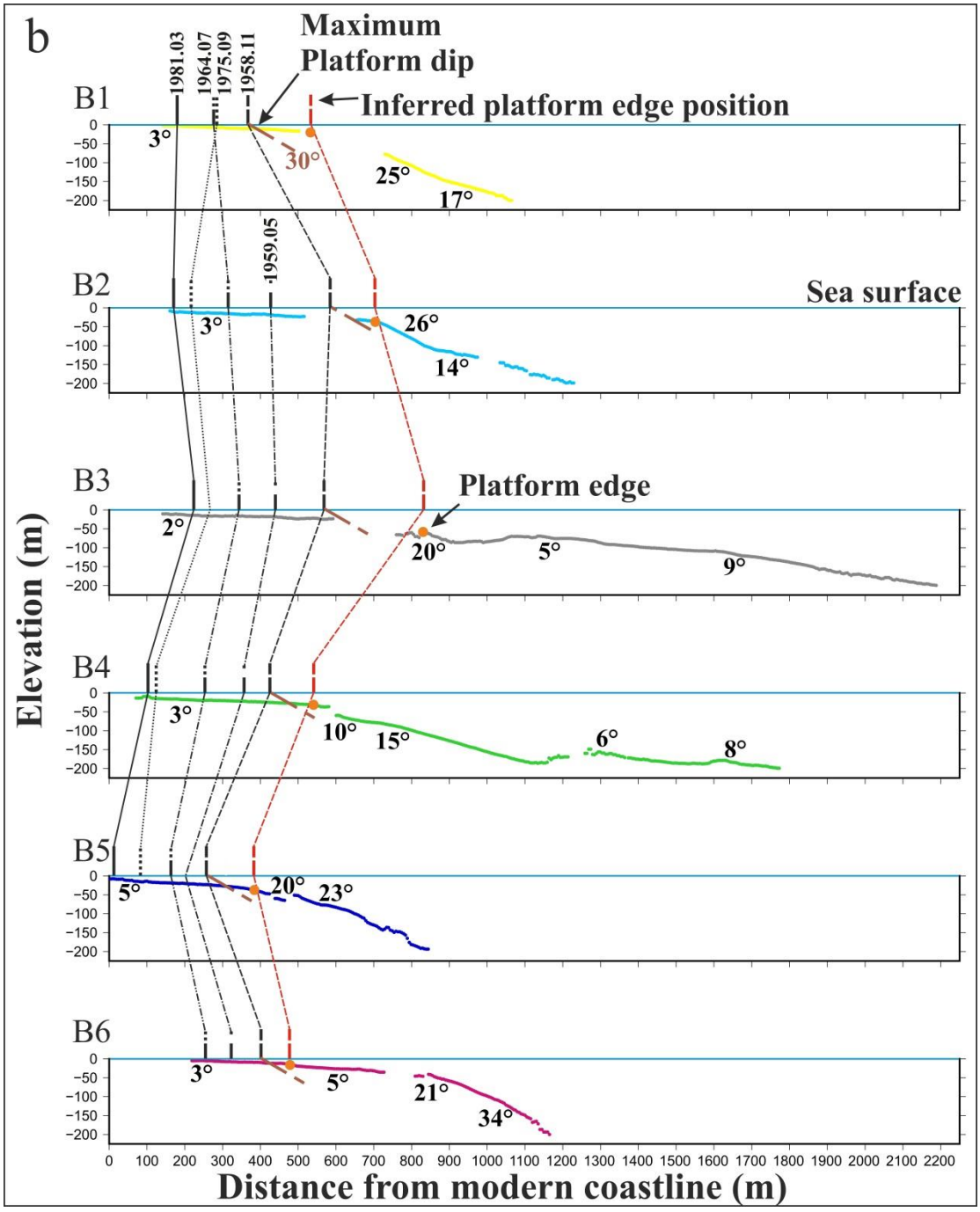

Figure 6(b). Bathymetric cross-sections (data from 2003 and 2004) with historical coastline positions. Orange circles locate the inferred modern platform edge. Numbers are seabed gradients in degrees.

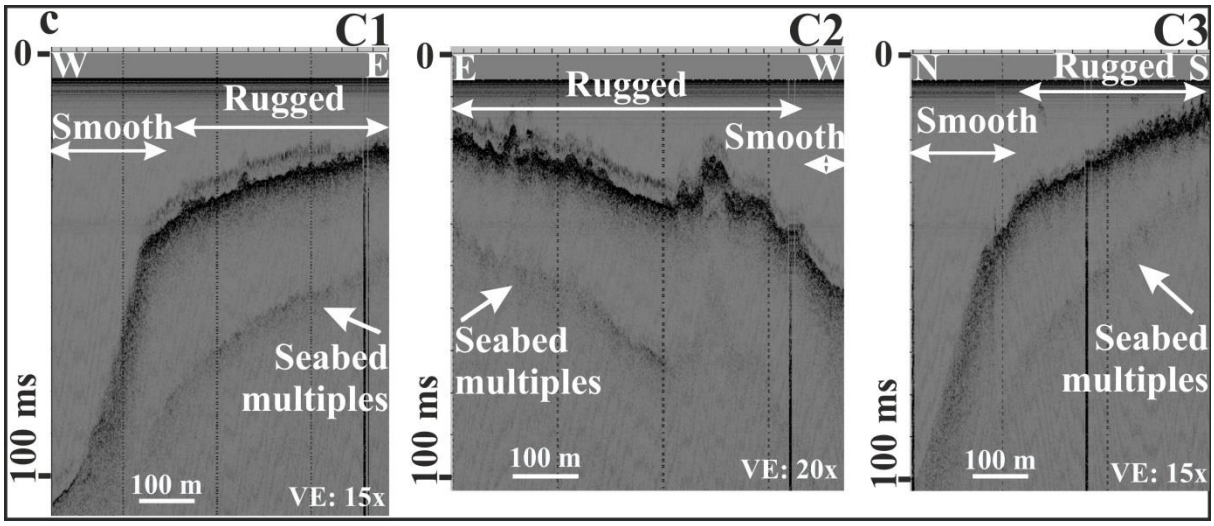

Figure 6(c). Chirp profiles illustrating the rugged morphology left behind after the erosion, and with smooth morphology below the platform. VE: vertical exaggeration.

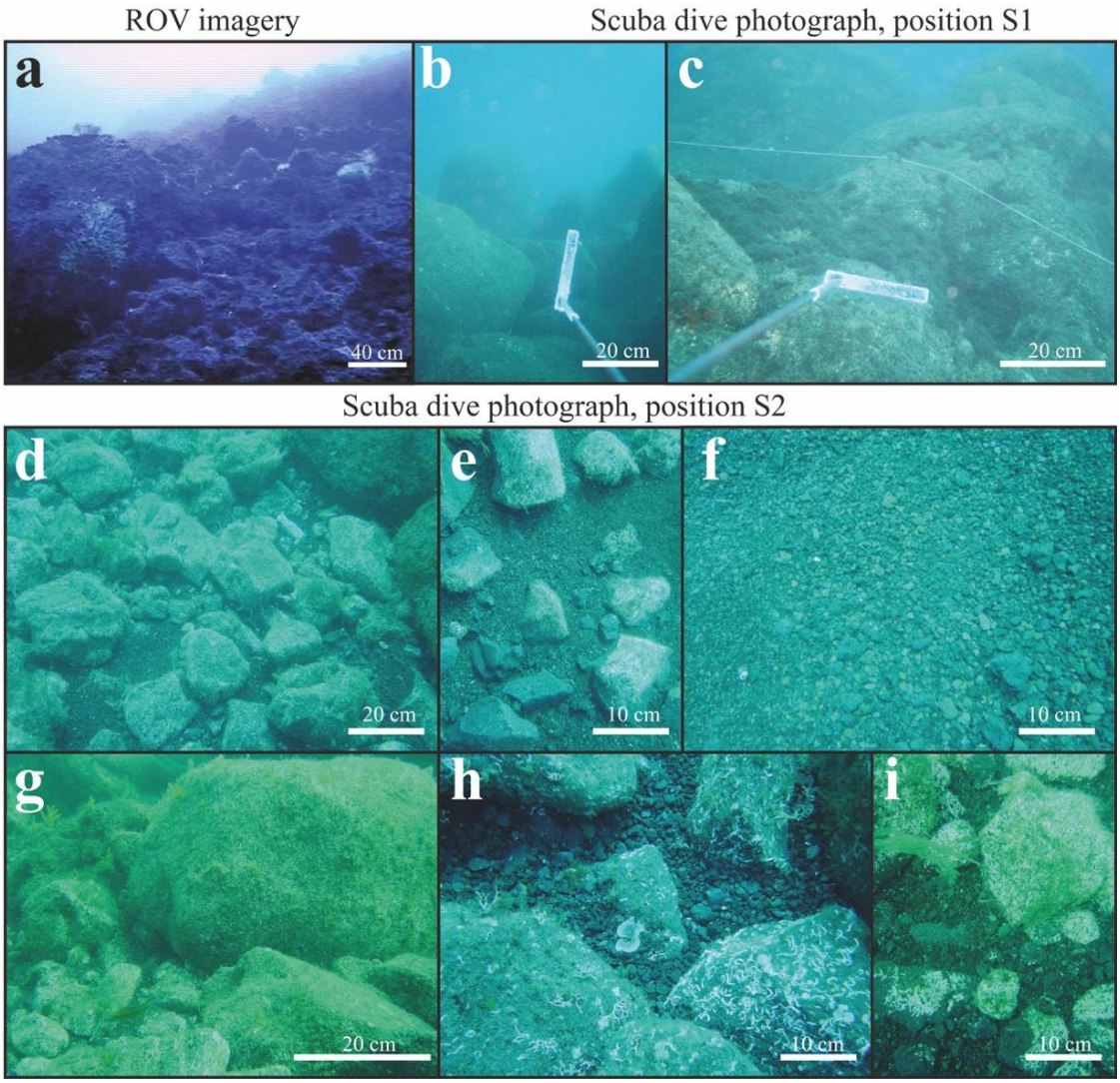

1222

1223 Figure 7. Seabed photographs located in Figure 6a. (a) ROV image showing
1224 a boulder field immediately below the platform edge to the northwest of
1225 Capelinhos (depth ~38 m). (b)-(c) SCUBA dive images from position S1
1226 (depth~10m) showing rounded boulders on the south platform. (d)- (i) SCUBA
1227 dive images from the submarine platform showing angular boulder to pebble-
1228 sized clasts (depth ~10 m).

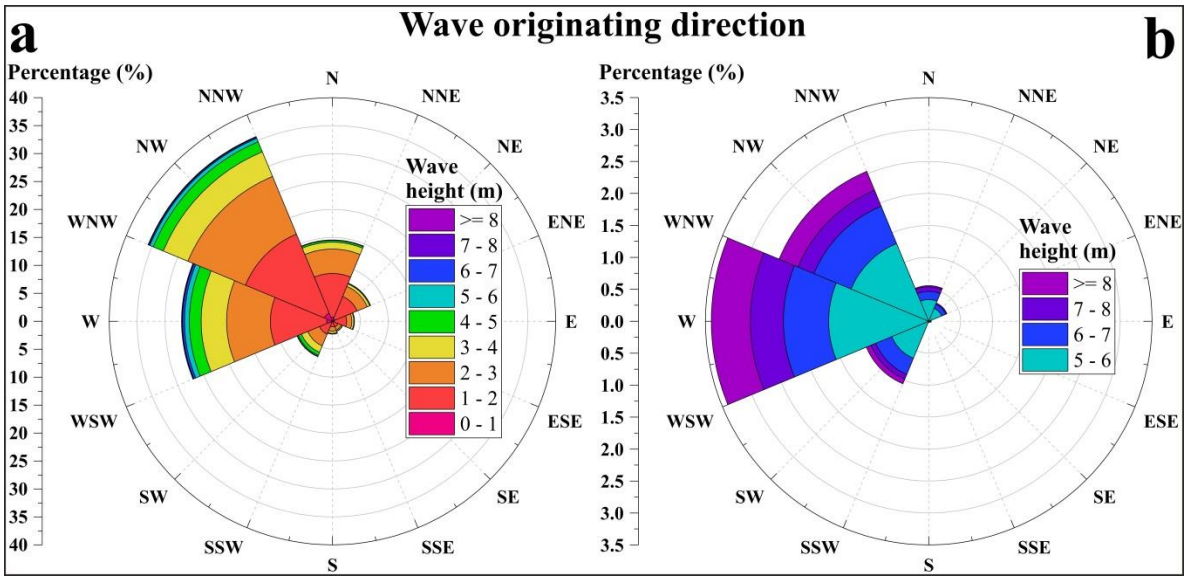

Figure 8. Offshore significant wave heights in the Capelinhos area derived from hindcasts by Carvalho (2003) for (a) all waves and (b) only waves above 5 m height.

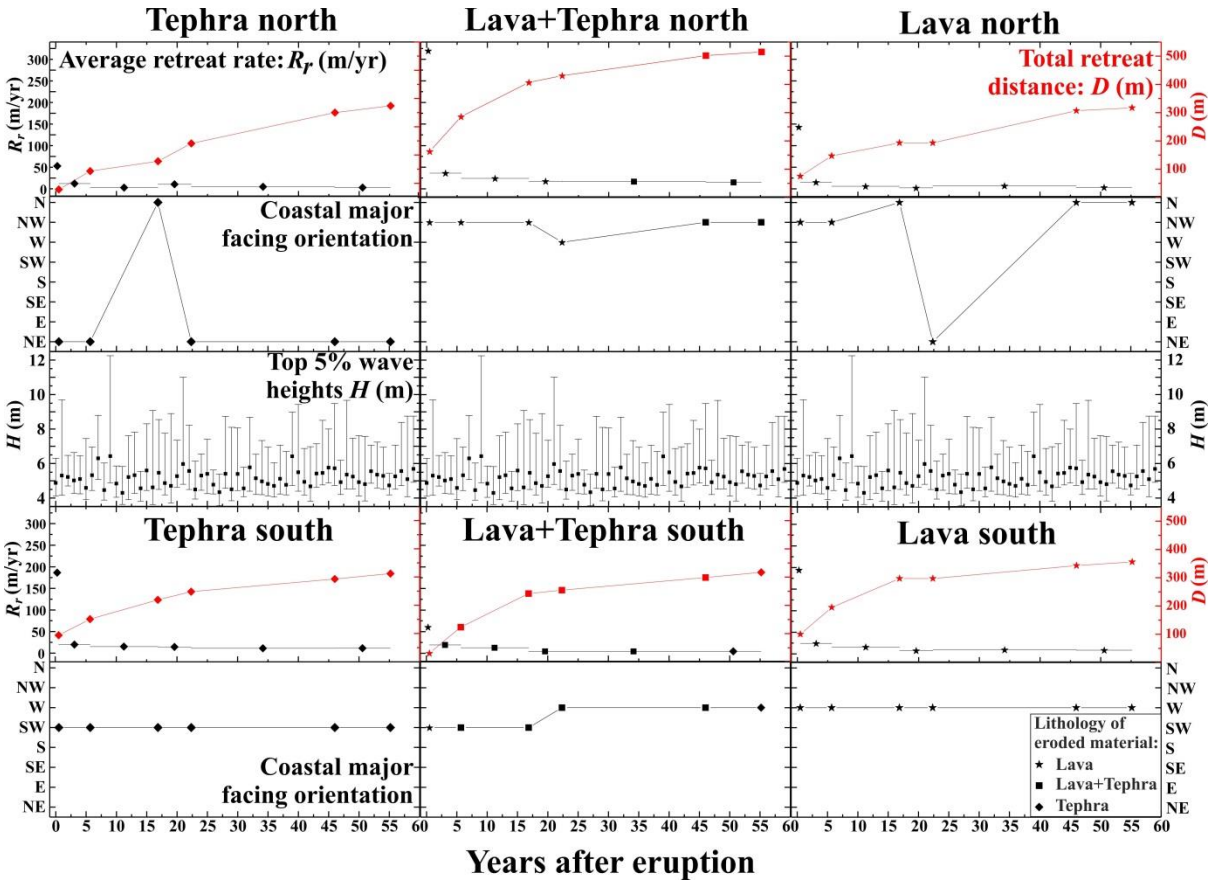

1234

1235 Figure 9. Comparison of retreat rates and distances with varying coastline
1236 orientations and extreme wave heights. In the upper graphs, black data
1237 represent the average retreat rate in different periods and red data represent
1238 the cumulative retreat distance. Coastal major facing orientation was worked
1239 out using the history of coastline change.

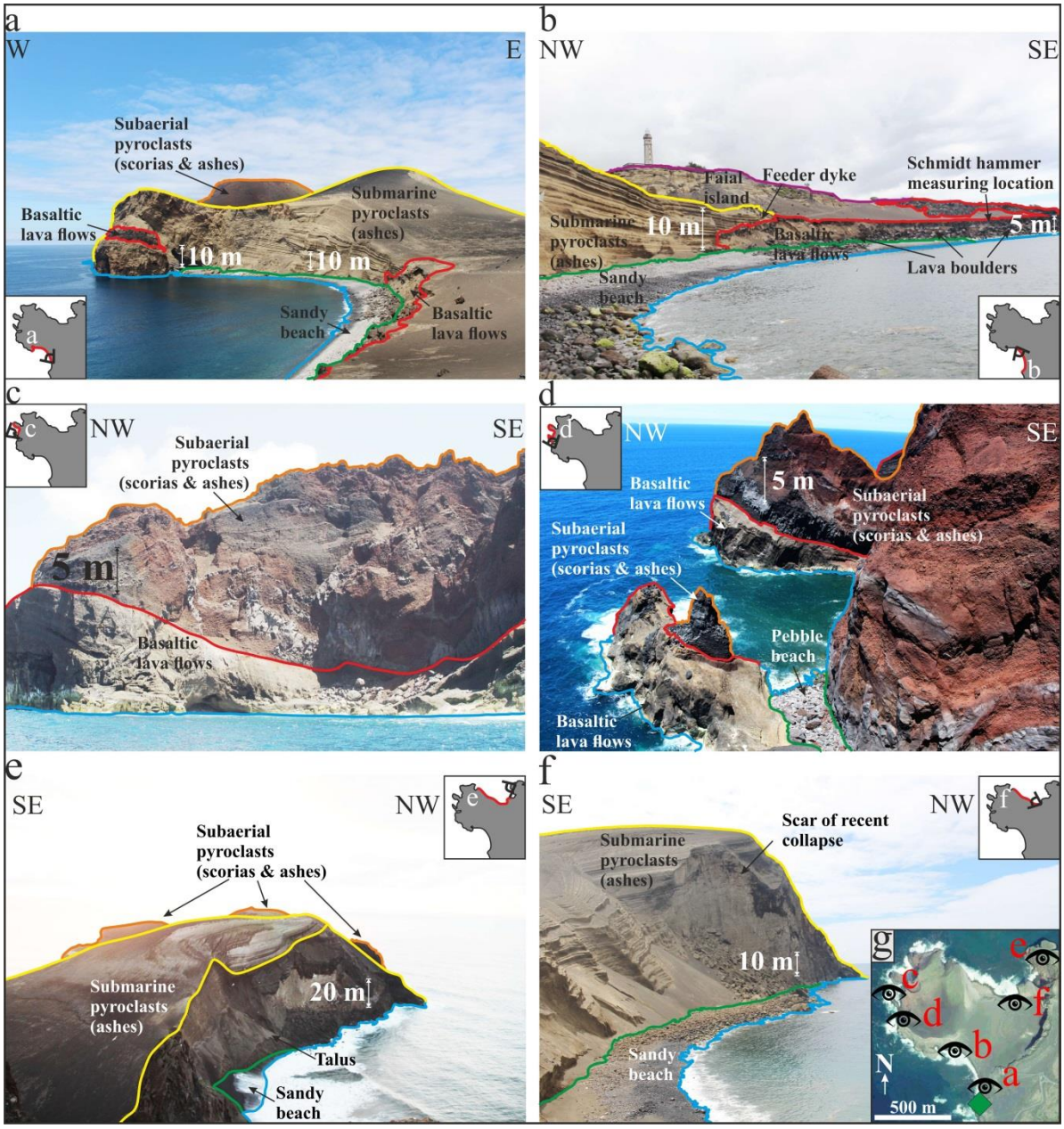

1240

1241 Figure 10. Photographs of Capelinhos coastal cliffs (in insets, red lines locate
1242 the exposed cliffs and black angles indicate the camera orientations). Blue
1243 lines mark the water lines, green lines mark the upper boundaries of sandy
1244 beaches, red lines delimit the basaltic lava flows, orange lines show the upper
1245 boundaries of the subaerial pyroclasts and yellow lines show the upper
1246 boundaries of the submarine pyroclasts. (a) Southwest coast of Capelinhos.

Note the strata of submarine pyroclasts dipping landward with a steep gradient (up to 30°) becoming nearly horizontal towards the easterly edge of the photo. The marked basaltic lava flows in the far left is part of two sea stacks that existed before the Capelinhos 1957/8 eruption. They are currently being re-exposed by marine erosion (Forjaz, 2007). (b) Outcrop on the south coast of Capelinhos with the paleo-cliff of Costado da Nau in the background below the lighthouse. NW cliff in the image contains horizontally bedded pyroclastic strata formed from hydromagmatic eruptions. SE cliff contains a basaltic lava flow (distinguished from the overlying feeder dyke). Note in far right large angular lava boulders at the base of the cliff caused by collapse of the overlying lava flow. (c) Offshore view (taken in 2011) of the westernmost cliff facing west showing a lower basaltic lava flow apparently lacking joints or faults and topped by red iron-rich subaerial pyroclasts. (d) Westernmost cliff of (c) in 2017. (e) Pyroclastic cliffs on the north coast (taken in 2011). Note in bottom-centre the talus in the cliff base formed by cliff collapse. (f) Cliff northeast of (e) in 2017. Note in far-centre the scar of a recent cliff collapse. (g) Locations where photos (a) – (f) were taken (background from google.com). Green diamond locates site of Schmidt hammer measurements.

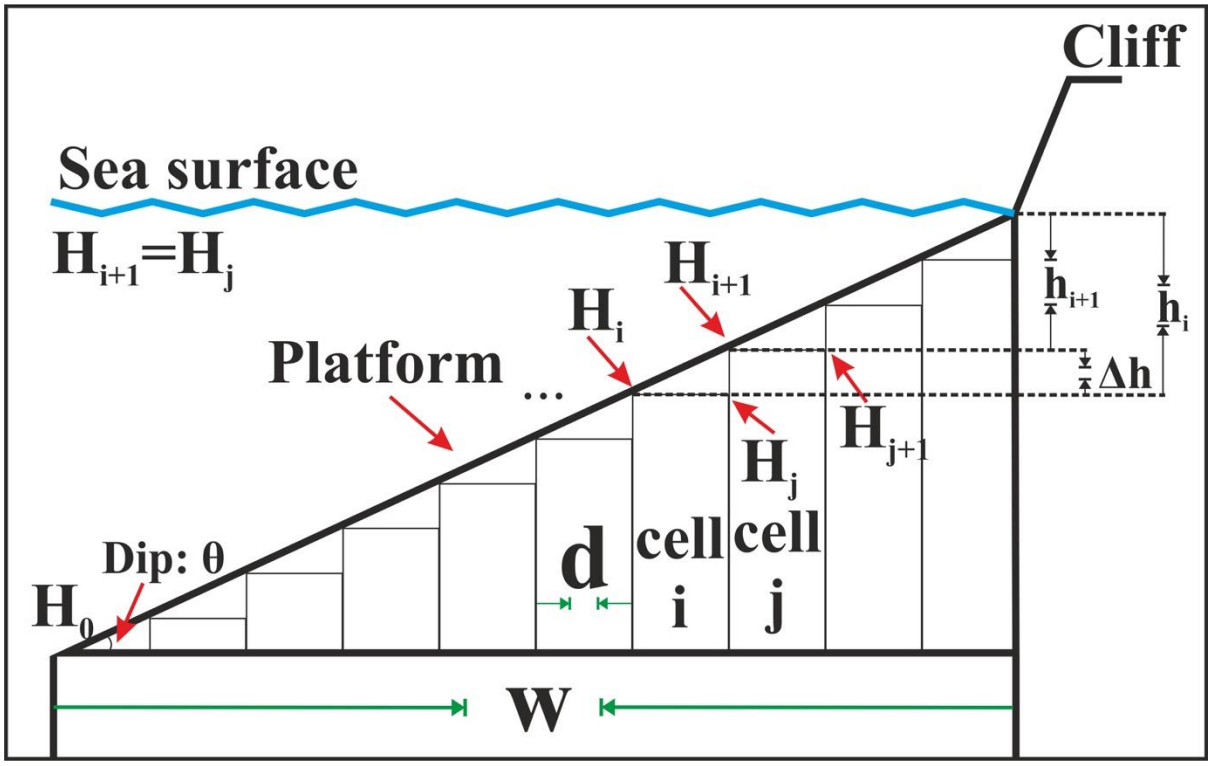

Figure 11. Geometry used in finite-difference wave attenuation model in which the platform is approximated by a series of horizontal cells.

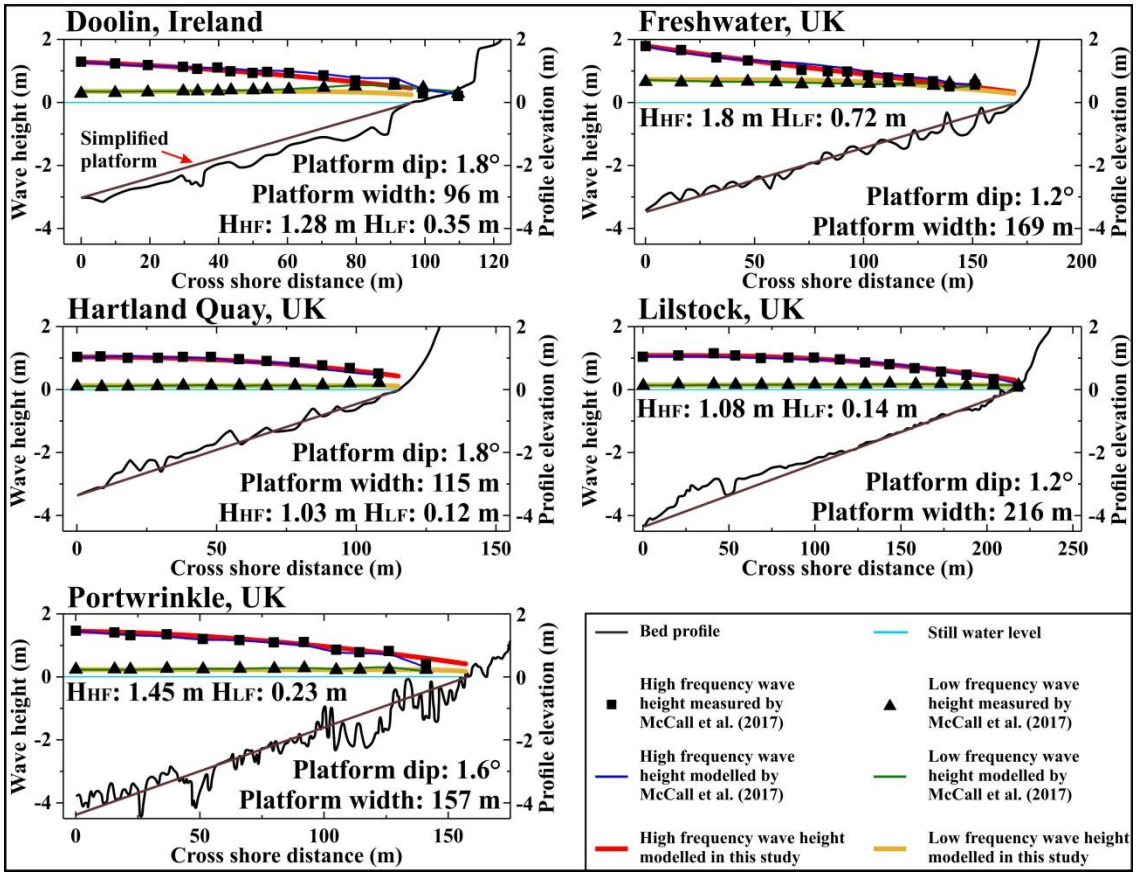

Figure 12. Comparison of observed wave height transformations over dipping platforms from McCall et al. (2017) with our finite-difference model predictions for high frequency (incident-band) and low frequency (infragravity). Split frequencies of 0.033 Hz (for Doolin, Freshwater, Hartland Quay and Portwrinkle) and 0.055 Hz (for Lilstock) were used to separate low frequency and high frequency motions. The model predictions of McCall et al. (2017) are also shown.

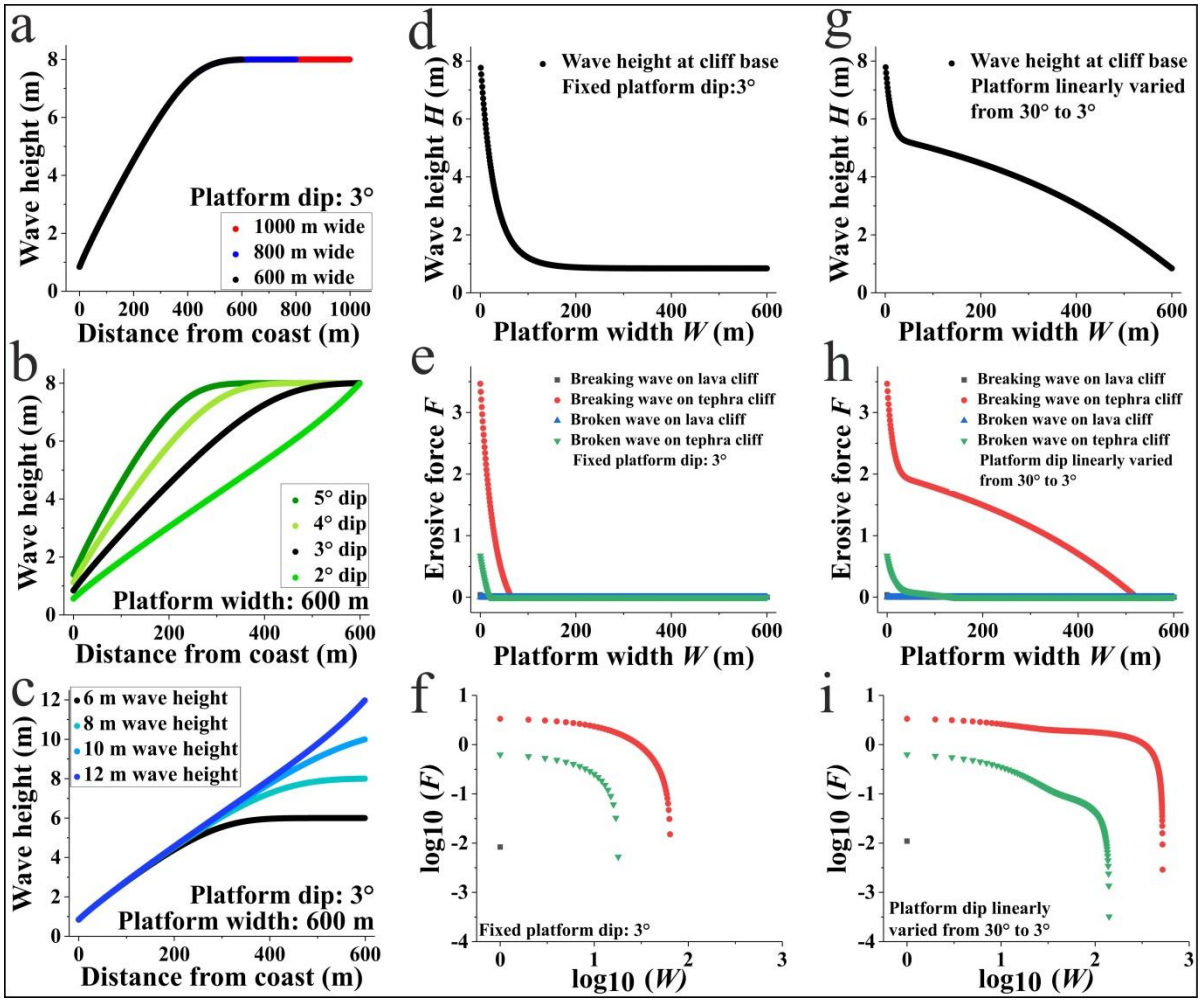

Figure 13. Simulations of effects of wave attenuation over dipping platforms of comparable dimensions to those of Capelinhos, using a cell size of 1 m. (a) Attenuated wave heights across platforms with varied widths marked in key. Wave height at platform edge is 8 m (critical wave height in appendix 6) and platform dips 3° (average dip in Table 2) seawards in direction of incoming waves. (b) Attenuated wave heights across dipping platforms with the varied platform dip angles marked. Wave height at platform edge is 8 m and platform width is 600 m (average platform widening distance in Table 2). (c) Attenuated wave heights across a dipping platform with the varied wave heights at the

platform edge marked. Platform width is 600 m and platform dips 3°. (d) and (g) Variation of platform dip and wave height at the cliff base with platform width up to 600 m. Wave height at platform edge is 8 m. (e) and (h) Graphs of wave erosive force F for breaking and broken wave on lava and tephra cliff against platform width. (f) and (i) logarithmic graphs of (e) and (h). Note in (e) and (h) curves for broken waves on lava cliffs are obscured because they are overlain by the curves for breaking waves on lava cliffs. In (f) and (i) curves for broken waves on lava cliffs were unplottable to plot due to the logarithmic axis (zero values).

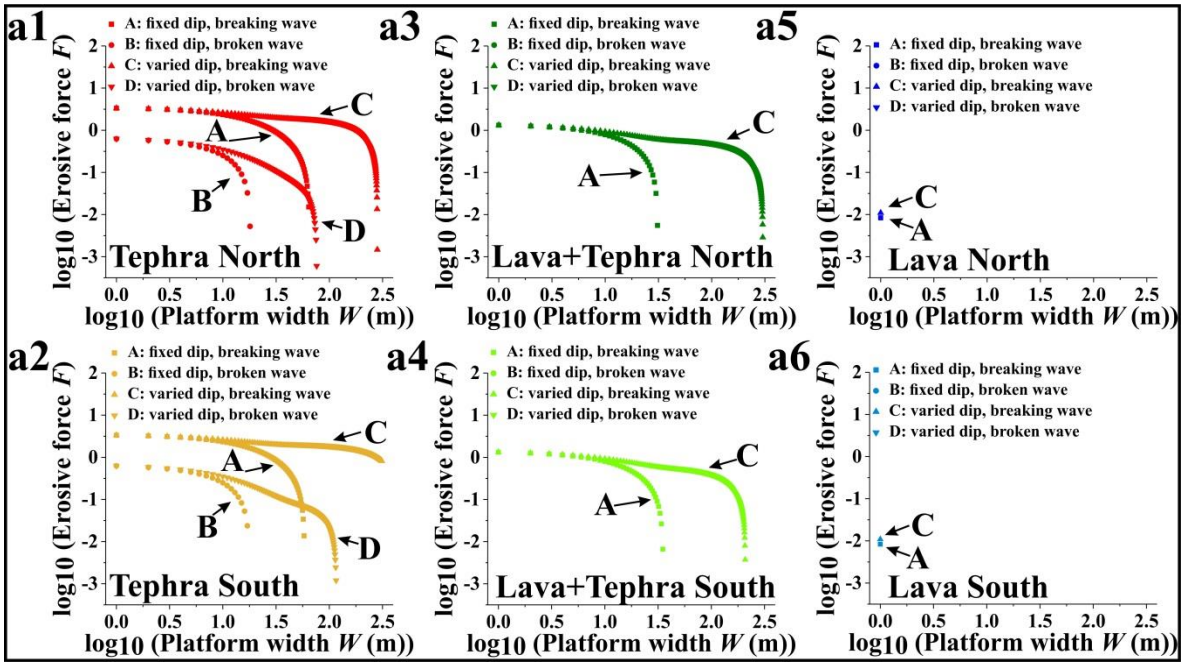

Figure 14. Simulations of erosive force for six different coastal sectors using a cell size of 1 m (corresponding simulations of wave height are shown in Appendix 8). The initial conditions were obtained from the interpreted geometry in Figure 6b (values in Table 2) for different coastal sectors and

extreme wave conditions in Appendix 7a (wave height at platform edge is 8 m which is the average height of top 5 percentile wave conditions). (a1)-(a6) Logarithmic graphs showing how model wave erosive force for breaking and broken waves varies with platform width for six coastal sectors. The following compressive strengths were used: lava cliff 51.6 MPa from this study, tephra cliff 12 MPa and lava+tephra cliff of 22.4 MPa from appendix 6). For the A and B curves, models were run with a constant 3˚ dip. For C and D, models were run with dip varying from 30˚ to 3˚. Note in a3-a6, curves B and D for broken waves were unplottable due to the logarithmic axis (zero values).

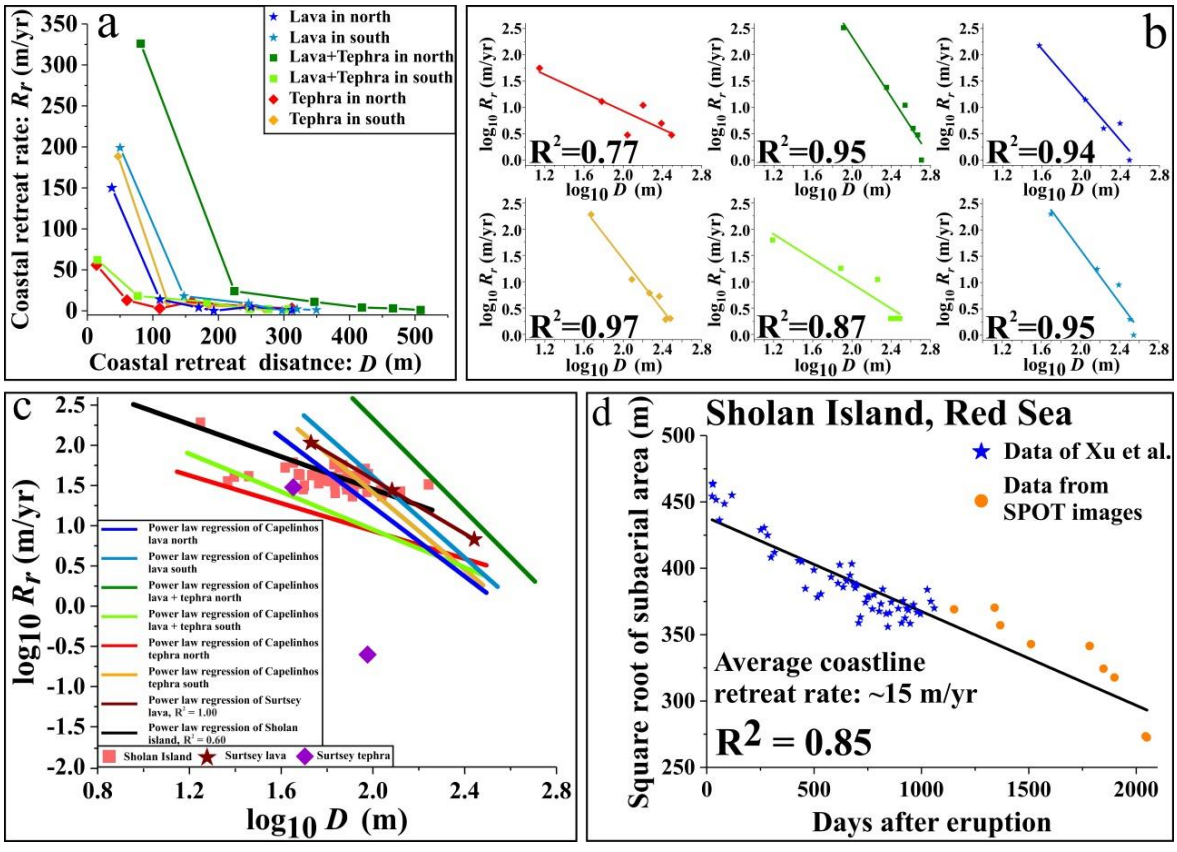

Figure 15. Relationships between coastal retreat rates (R_r) and coastal retreat

distance (*D*) derived from the data in Figure 9. (a) Retreat rates versus the coastal retreat distance for the six different coastal sectors (data in Table 1). (b) The data plotted with two logarithmic axes revealing inverse power law relationships for the six different coastal sectors. (c) Relationships of (b) combined and compared with those for (brown line) Surtsey Island (for the period 1963–2012 from data of Romagnoli and Jakobsson (2015), see Table A2 for calculations) and (black line) Sholan Island (for the period 2011-2017, data derived from (d)). (d) Post-eruptive areal changes of Sholan Island in the Red Sea illustrating the early evolution not recorded at Capelinhos or Surtsey. See Appendix 5 and Table A4 for images and interpreted coastlines.

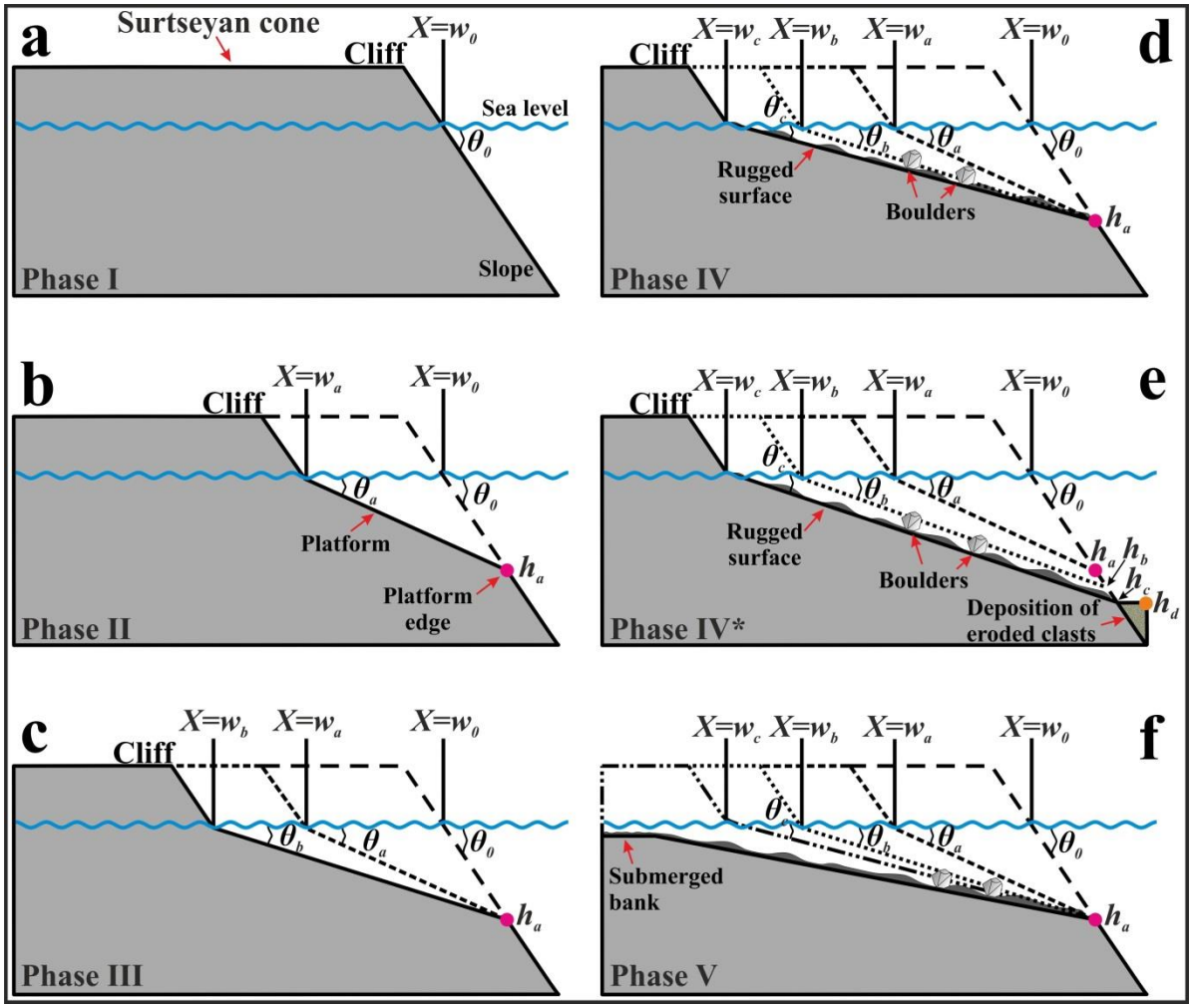

1322

1323 Figure 16. Suggested submarine platform development by erosion of
1324 Surtseyan cones. (a) The seaward flank of the Surtseyan cone was attacked
1325 by waves during the eruption. (b) Erosion of the Surtseyan cone progressively
1326 created a submarine platform. (c) Further widening and deepening of the
1327 platform with time. (d) Rugged surface left after erosion and covered with
1328 boulders. In this case all eroded material was deposited at depth beyond the
1329 submarine slope (below the shelf edge), hence *ha* lies on the original slope of
1330 (a). (e) Based on the profiles in Figure 6b, deposition of eroded clasts on the
1331 uppermost slope likely extended (prograded) the platform edge as marked by

1332 h_d. (f) How the present subaerial part of the Surtseyan cone could eventually
1333 be removed by erosion. The horizontal positions of cliff base in stages I-IV are
1334 represented as w_0, w_a, w_b and w_c. Symbols θ_0 - θ_c represent the dips of
1335 platform in stages I-IV. h_a-h_c are depths of platform edge in stages I-IV.

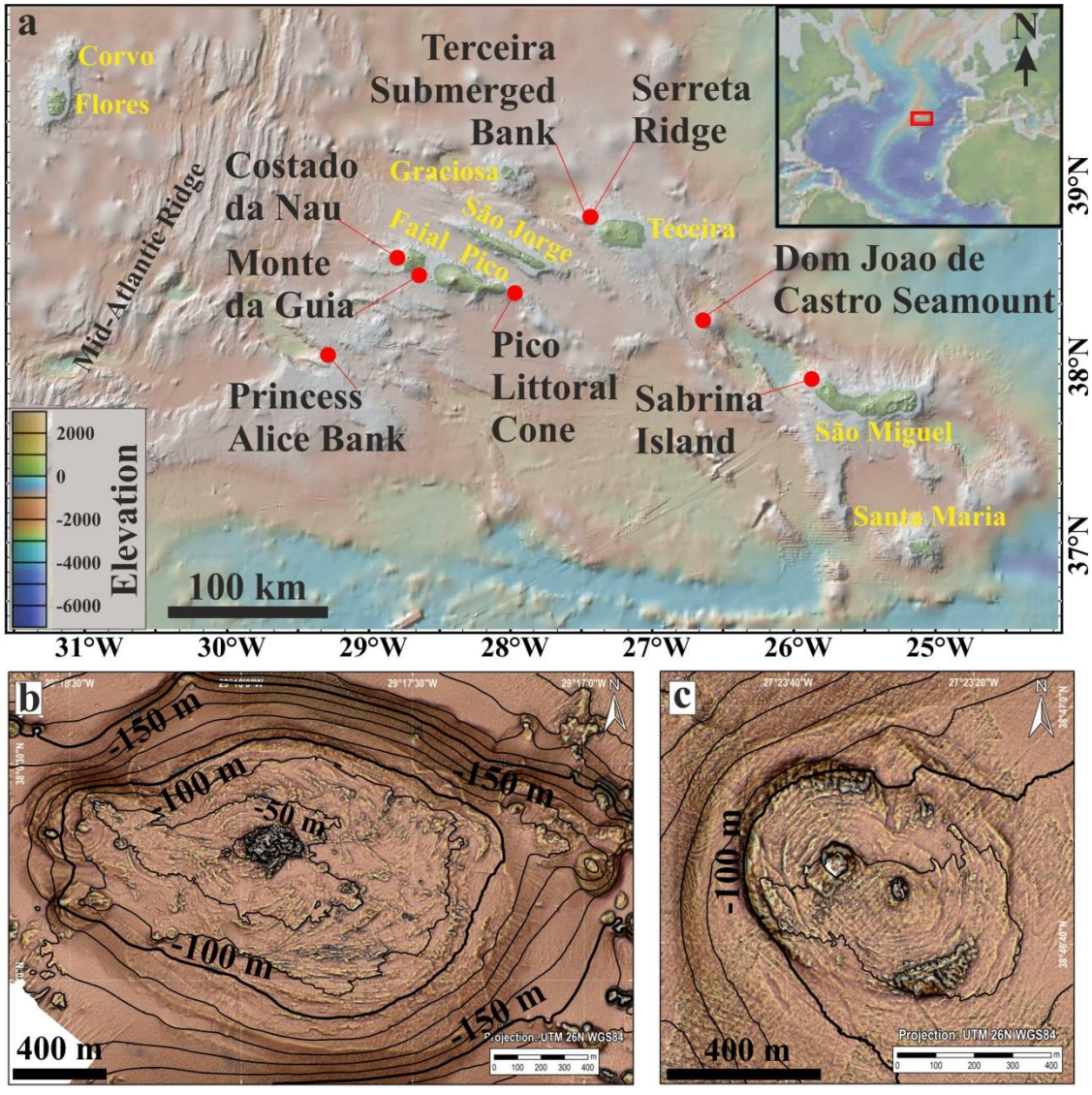

1336

1337 Figure 17. Azores submerged banks of likely Surtseyan origin in multibeam
1338 bathymetry data (contour interval 10 m and highlighted every 50 m). (a)
1339 Locations of submerged Surtseyan cones. Submarine bathymetry and

subaerial elevation data are from Global Multi-Resolution Topography Data Synthesis (GMRT) of GeoMapApp (Ryan et al., 2009). (b) Top of the Princess Alice Bank exhibiting a main Surtseyan cone in the centre and a smaller cone to the left. Roughly concentric fine ridges on the bank likely represent different stages of pyroclastic deposition throughout the eruption and effects of varied resistance to erosion of the strata. (c) Submerged bank to the northwest of Terceira Island exhibiting two adjacent extrusion centres and concentric fine ridges.

1349 **Tables:**

Table 1. Coastal retreat rates, areal changes and retreat distances for various coastal sectors of Capelinhos for the period 11958.11 – 2014.10. Values for incomplete coast are marked with *.

Coastal Sector	Date *T*	Time interval *ΔT* (yr)	Elapsed time after eruption	Areal change *ΔA* (m^2)	Average coastline length *L'* (m)	Coastal retreat distance *ΔD* (m)	Total Coastal retreat distance *D* (m)	Average retreat rate: R_r (m/yr)
Tephra north	1958.11-1959.05	0.5	0.5	9538	340	28	28	56
	1959.05-1964.07	5.17	5.67	24179	370	65	93	13
	1964.07-1975.09	11.17	16.84	14358	416	34	128	3
	1975.09-1981.03	5.5	22.34	28396	450	63	191	11
	1981.03-2004.11	23.67	46.01	68130	627	109	300	5
	2004.11-2014.10	9.17	55.18	21120	868	24	324	3
Tephra south	1958.11-1959.05	0.5	0.5	40183	426	94	94	188
	1959.05-1964.07	5.17	5.67	28453	498	57	151	11
	1964.07-1975.09	11.17	16.84	37905	560	68	219	6
	1975.09-1981.03	5.5	22.34	12360	427*	29	248	5
	1981.03-2004.11	23.67	46.01	23602	523*	45	293	2
	2004.11-2014.10	9.17	55.18	11163	609*	18	312	2
Lava + Tephra north	1958.11-1959.05	0.5	0.5	39950	245	163	163	326
	1959.05-1964.07	5.17	5.67	25249	205	123	286	24
	1964.07-1975.09	11.17	16.84	21956	182	121	407	11
	1975.09-1981.03	5.5	22.34	4588	195	24	431	4
	1981.03-2004.11	23.67	46.01	17561	246	71	502	3
	2004.11-2014.10	9.17	55.18	3461	262	13	515	1
Lava + Tephra south	1958.11-1959.05	0.5	0.5	22285	724	31	31	62
	1959.05-1964.07	5.17	5.67	57477	625	92	123	18
	1964.07-1975.09	11.17	16.84	66292	557	119	242	11
	1975.09-1981.03	5.5	22.34	6696	561	12	254	2
	1981.03-2004.11	23.67	46.01	24705	551	45	299	2
	2004.11-2014.10	9.17	55.18	10756	597	18	317	2
Lava north	1958.11-1959.05	0.5	0.5	72788	970	75	75	150
	1959.05-1964.07	5.17	5.67	51365	715	72	147	14
	1964.07-1975.09	11.17	16.84	27092	586	46	193	4
	1975.09-1981.03	5.5	22.34	0	548	0	193	0
	1981.03-2004.11	23.67	46.01	45501	402	113	307	5
	2004.11-2014.10	9.17	55.18	2613	241	11	317	1
Lava south	1958.11-1959.05	0.5	0.5	12196	122	100	100	199
	1959.05-1964.07	5.17	5.67	10220	107	95	195	18
	1964.07-1975.09	11.17	16.84	16211	158	102	297	9
	1975.09-1981.03	5.5	22.34	0	212	0	297	0
	1981.03-2004.11	23.67	46.01	6784	148	46	343	2

	2004.11-2014.10	9.17	55.18	985	79	12	356	1
Average of all sectors	1958.11-1959.05	0.5	0.5	196940	2827	82	82	164
	1959.05-1964.07	5.17	5.67	196943	2520	84	166	16
	1964.07-1975.09	11.17	16.84	183813	2458	82	248	7
	1975.09-1981.03	5.5	22.34	52040	2393	21	269	4
	1981.03-2004.11	23.67	46.01	186283	2497	72	341	3
	2004.11-2014.10	9.17	55.18	50098	2656	16	357	2

Table 2. Geometry of platforms on selected bathymetric cross-sections (Figure6 B1-B6).

Cross section	Coastal sector	Total platform width (m)	Platform edge depth (m)	Dip of platform (◦)
B1	Tephra north	533	22	3
B2	Lava north	703	36	3
B3	Lava+Tephra north	832	59	2
B4	Lava south	541	31	3
B5	Lava+Tephra south	383	38	5
B6	Tephra south	475	14	3

1361 **Appendices:**

Table A1. Root Mean Square Error of georeferencing and digitizing of maps.

Source	Historical shorelines	Resolution (dpi)	Reference scale	Root Mean Square Error (m)
Google Earth images	2004 and 2014	72	1:1,200	10.88
Historical map of Machado and Freire (1985)	1958, 1959, 1964, 1975 and 1981	68	1:1,200	39.44
Figure 5 in this study	1958, 1959, 1964, 1975, 1981, 2004 and 2014	600	1:500	41.01

Table A2. The digitised lengths of coastlines for different coastal sectors of Capelinhos for the period 1958 – 2014. Values for incomplete coast are marked with "*".

Date T				Digitised coastline length L (m)					
				Tephra north	Tephra south	Lava + Tephra north	Lava + Tephra south	Lava north	Lava south
1958.11-	T_a	1958.11	L_a	336	391	273	757	1134	135
1959.05	T_b	1959.05	L_b	343	462	216	691	805	110
1959.05-	T_a	1959.05	L_a	343	462	216	691	805	110
1964.07	T_b	1964.07	L_b	397	535	194	559	624	104
1964.07-	T_a	1964.07	L_a	397	535	194	559	624	104
1975.09	T_b	1975.09	L_b	436	584	169	555	548	212
1975.09-	T_a	1975.09	L_a	436	384*	169	555	548	212
1981.03	T_b	1981.03	L_b	465	469*	221	567	548	212
1981.03-	T_a	1981.03	L_a	465	469*	221	567	548	212
2004.11	T_b	2004.11	L_b	789	576*	272	535	256	84
2004.11-	T_a	2004.11	L_a	789	576*	272	535	256	84
2014.10	T_b	2014.10	L_b	946	641*	251	659	227	75

1362

Table A3. Coastal retreat rates, areal changes and retreat distances in Surtsey for different cliff rock types in the period 1963 – 2012 calculated from Figure 12 of Romagnoli and Jakobsson (2015).

Cliff rock type	Date	Retreat rate (m/yr)	Areal change (km^2)	Average retreat rate: R_r (m/yr)	Coastal retreat distance D (m)
Tephra and tuff	1964 - 1967	30	0.48 - 1	30	90
	1967 - 2006	0.2 - 0.3	0.4 - 0.48	0.25	99.75
Lava	1967 - 1968	75 - 140	1.8 - 1.9	107.5	107.5
	1969 - 1970	20 - 35	1.65 - 1.7	27.5	135
	1967 - 2012	1.5 - 12	0.8 - 1.65	6.75	418.5

1363

1364

Table A4. Root Mean Square Error from georeferencing and digitizing of Sholan Island satellite images.

Source	Historical shorelines	Spatial resolution (m)	Resolution in dots per inch	Reference scale	Root Mean Square Error (m)
Images from Xu et al. (2015)	2011.12-2014.11	30	4.23	1:5000	16.77
SPOT	2015.02-2017.07	2.5	101.6	1:10000	1.25

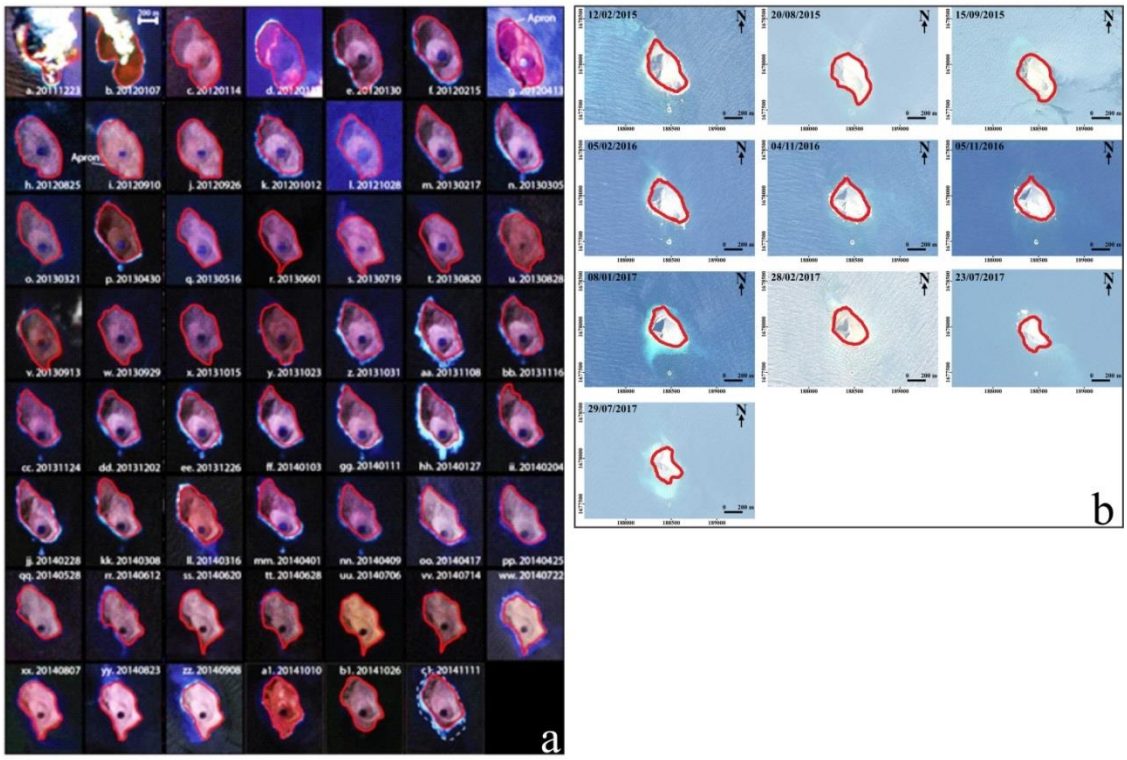

Appendix 5. Satellite images showing the 2011-2017 subaerial area of Sholan Island following the eruption. Coastline positions interpreted here are highlighted in red. (a) The images from EO-1, ALI, Landsat-7 and Landsat-8, typically with spatial resolutions of 30 m (Xu et al., 2015). (b) The images from SPOT with spatial resolutions of 2.5 m (esa.com).

Appendix 6.

Sunamura et al. (2014) specified an equation of Kahraman (2001) to estimate compressive strength S_c from cliff rock density and Schmidt hammer rebound values:

$$S_c = 6.97e^{0.014\rho R} \quad (1)$$

where S_c is the compressive strength in MPa, R is the Schmidt hammer rebound value, and ρ is the rock density of cliff material in g/cm^3.

Machado et al. (1962) estimated the density of lava and tephra from Capelinhos eruption as 2.6 g/cm^3 and 1.1 g/cm^3 respectfully. We averaged these rock densities for lava+tephra sector cliffs (1.85 g/cm^3). The average Schmidt hammer rebound value measured from Capelinhos lava cliff is 55. We used the average value of 35 for tephra from Kahraman (2001). The value of 45 for lava+tephra sectors was obtained by averaging the above values for lava and tephra materials.

The compressive strength S_c of lava, tephra and lava+tephra is then calculated as following from equation (1): Lava cliff: S_c = 51.6 MPa; Tephra cliff: S_c = 12.0 MPa; Lava+Tephra cliff: S_c = 22.4 MPa.

Using the critical wave height equation of Sunamura (1992) for cliff erosion:

$$H_{crit} = \frac{S_c}{\rho g} e^{-\Gamma} \quad (2)$$

where S_c is the comprehensive strength of cliff material, ρ is the density of seawater (1025 kg/m3), g is the gravity acceleration (9.8 m/s2) and Γ is a

constant ($\Gamma = \ln\frac{A}{B}$) , A and B are constants and B/A=ε=0.0015 for breaking waves or 0.0040 for broken waves (Sunamura et al., 2014).

From the comprehensive strength S_c for cliffs with different lithologies calculated above, we estimated the wave height threshold to initiate the cliff erosion for lava, tephra and lava+tephra cliffs under the attack of breaking and broken waves:

Lava cliff: a) breaking wave: H_{crit} = 7.7 m; b) broken wave: H_{crit} = 20.5 m;

Tephra cliff: a) breaking wave: H_{crit} = 1.8 m; b) broken wave: H_{crit} = 4.8 m;

Lava+Tephra cliff: a) breaking wave: H_{crit} = 3.3 m; b) broken wave: H_{crit} = 8.9 m.

Hence, wave heights >5 m are likely to exceed the critical wave height allowing even broken waves to erode tephra cliffs. Wave heights >8 m were used in the numerical modelling part (Figures 13 and 14 and appendix 8) as 8 m heights yield the critical wave height (breaking wave) of all cliff materials and dominate initiate coastal erosion.

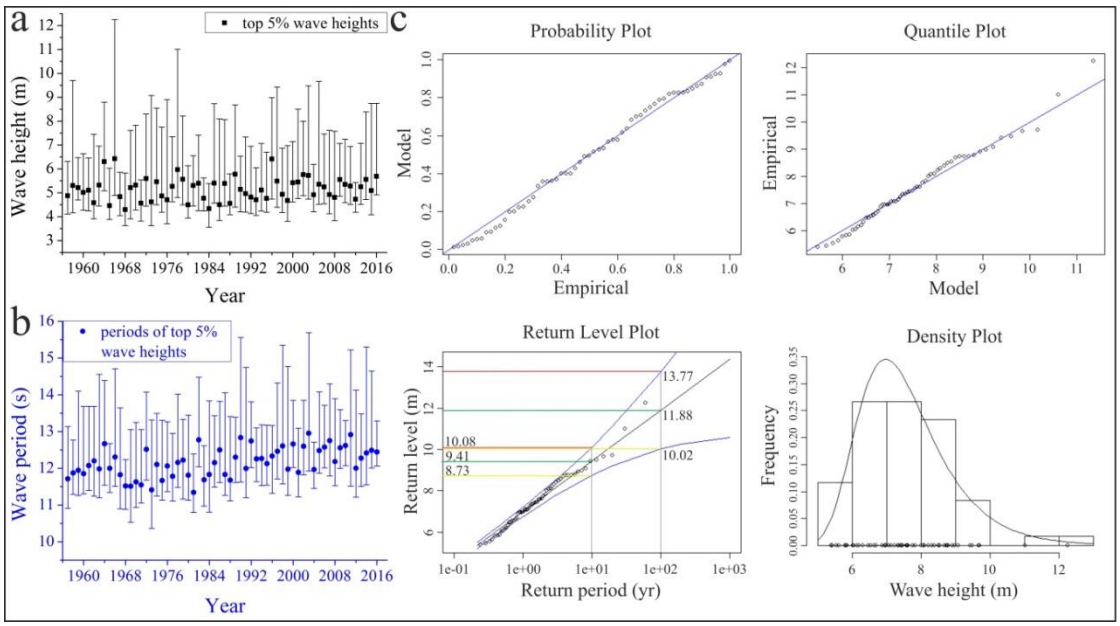

1417

1418 Appendix 7. Extreme wave properties for the period 1957 – 2016 for a sea
1419 position adjacent to Capelinhos (38.625°N, 28.875°W) derived from ERA–40
1420 and ERA–Interim outputs (Uppala, 2005; Dee, 2011). (a) For times when
1421 significant wave heights were in the top 5 percentile, solid circles represent
1422 their average heights and black bars show the range of heights. (b) For the
1423 same data durations as in (a), blue-filled circles represent their mean periods
1424 and blue bars the range of periods. (c) Diagnostic plots of generalised
1425 extreme value fit to extreme wave conditions modelled from the 60 maxima in
1426 the 1957 to 2016 extreme wave heights. The probability plot (top left panel)
1427 and quantile plot (top right panel) compare the simulated values to the
1428 empirical values. A return level plot (bottom left panel) indicates the expected
1429 extreme wave heights for different return periods. The density plot (bottom
1430 right panel) is the histogram of the extreme quantile against its probability
1431 (Tank et al., 2009; Lee, 2014).

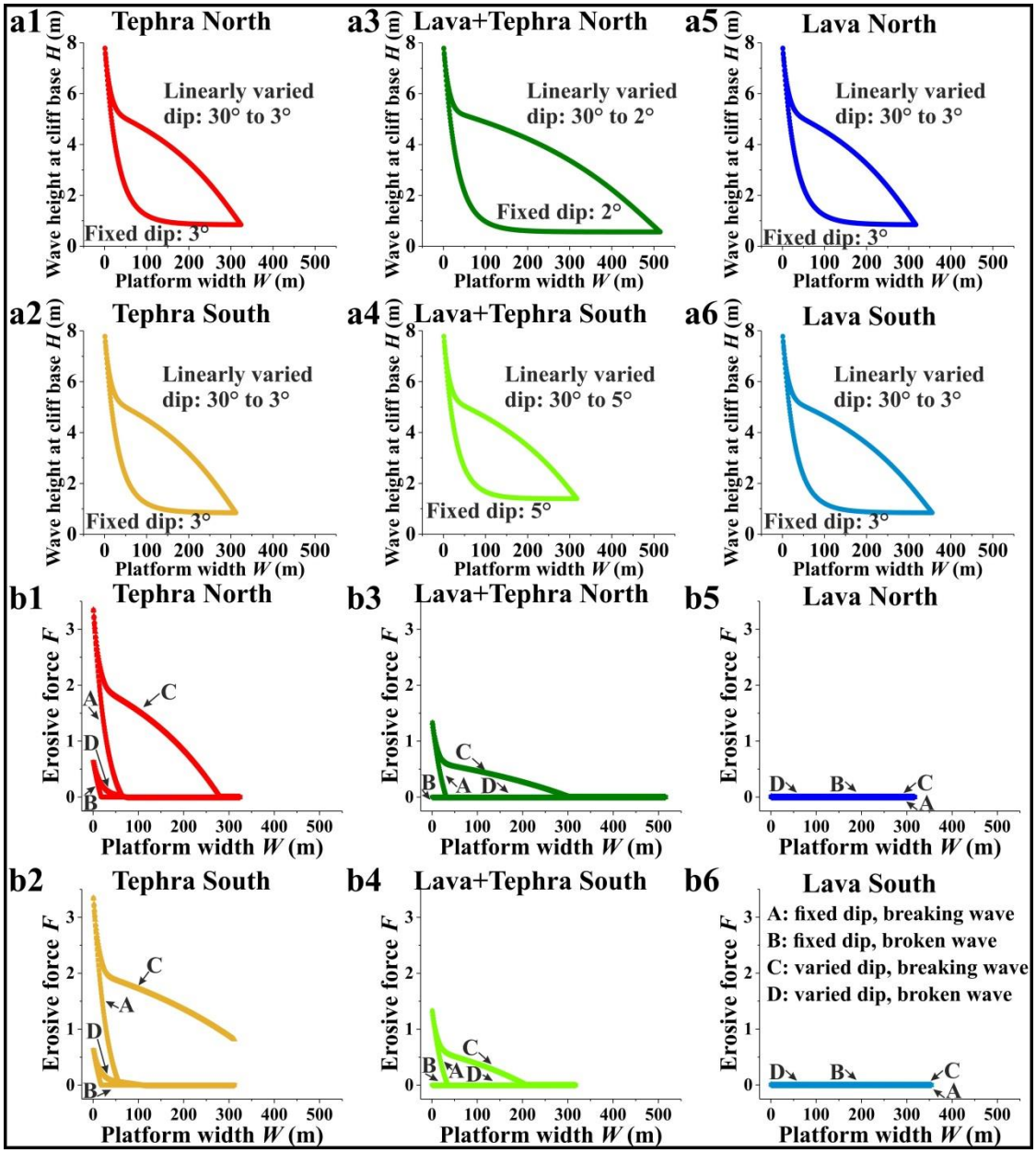

1432

1433 Appendix 8. Simulations of wave height and erosive force for six different
1434 coastal sectors using a cell size of 1 m. (a1-a6) Variation of wave height at
1435 cliff base with respect to platform width for six coastal sectors. (b1-b6)
1436 Graphs of wave erosive force for breaking and broken waves on six coastal
1437 sectors using attenuated wave heights from a1-a6. The colour scheme follows
1438 the one of Figures 14 and 15.